J. Fluid Mech. (1992), *vol.* 238, *pp.* 337–369
Printed in Great Britain

A hydroelastic model of macromechanics in the endolymphatic vestibular canal

By R. D. RABBITT AND E. R. DAMIANO†
Department of Mechanical Engineering, Washington University, St. Louis, MO 63130, USA

(Received 4 February 1991 and in revised form 21 October 1991)

A hydroelastic model describing the mechanics of the human semicircular canal is presented that extends previous work to address the influence of the shape of the labyrinth and the interaction between the endolymph and the cupula. The analysis is based extensively on the three-dimensional geometry and structure of the system and exploits the slender toroidal geometry to obtain an asymptotic solution describing the velocity distribution of the endolymph, the pressure distribution and the deflection of the cupula. All parameters appearing in the model are explicitly defined in terms of physical properties and the geometry. Results for the structure of an infant human endolymphatic canal agree well with experimental measurements of the end-organ velocity gain and phase over the entire physiological range of angular head frequencies. From 0.09 to 1.5 Hz the mechanical response relative to head velocity is essentially constant and the end-organ acts as an angular velocity transducer. Below 0.09 Hz the velocity gain is diminished and above 1.5 Hz the velocity gain is enhanced. For a 1 rad sinusoidal rotation of the head, the analysis predicts an average cupula displacement for the infant canal of approximately 8×10^{-5} cm at 0.09 Hz and 2×10^{-3} cm at 2.0 Hz.

1. Introduction

It is often suggested that our sixth sense may be attributed to human intuition, which, strictly speaking, falls into the realm of extrasensory perception. It is not necessary, however, for one to look beyond our own physical being to see that indeed we do possess a sixth sensory capability which is as 'earthly' as the five better known special senses. As vital as it is to the homeostasis of dynamical equilibrium, the vestibular system is frequently taken for granted owing to the inconspicuous nature of its function. Nonetheless, the functional importance of the vestibular system suggests that it should be classified as one among the primary special senses with which we are commonly familiar.

Fundamental to the ability to control the eyes and to maintain equilibrium, the human semicircular canals provide the body with the ability to sense angular motion of the head. This sensory system consists of a fluid-coupled structure that induces a motion-sensitive signal on the vestibular nerve. Experimental measurements of the afferent neural response show that the system acts as an angular velocity transducer over a broad range of physiological rotational frequencies (Fernandez & Goldberg, 1971; Wilson & Jones 1979). In the middle frequency range the neural signal is proportional to, and in phase with, the angular velocity of the head. At low frequencies the signal on the vestibular nerve shows a diminished firing rate and a

† Current address: Department of Mathematical Sciences, Rensselaer Polytechnic Institute, Troy, NY 12180, USA.

phase lead relative to head velocity. In contrast, an enhanced firing rate is observed at high frequencies in combination with a phase lead. This neural response is governed by the mechanics of the vestibular end organ and by the mechano-electrical transduction of the sensory hair cells. The geometry and structure of the semicircular canals play an important role in the process.

In this work we analyze the mechanical response by investigating the dynamic interaction of the endolymphatic fluid in the semicircular canal with the innervated cupula partition. Results for the geometry of an infant human indicate that the deflection of the cupula closely follows the firing rate measured on the vestibular nerve over the entire physiological frequency range. This includes the enhancement of the velocity gain and the phase lead existing on the vestibular nerve at high physiological frequencies not predicted by previous mechanical models.

2. Anatomy and physiology of the end organ

Located within the temporal region of the skull is a bony labyrinthine system which consists of three semicircular canals lying in planes which are approximately mutually orthogonal. Housed within this labyrinth and suspended in perilymphatic fluid is a membranous duct which itself contains a fluid known as endolymph. The composition of the fluids plays an important role in the transduction process by the sensory hair cells (Corey & Hudspeth 1979; Ohmori 1985; Bell & Holmes 1986).

The endolymphatic duct consists of two specialized types of sensory systems, the semicircular canals and the otolith organs. The former is sensitive primarily to angular motion of the head while the latter responds primarily to linear motion. The three semicircular ducts converge upon the utricle which provides fluid continuity among the three canals. The utricle contains the utricular macula which comprises part of the sensory apparatus of the otolith organs. The rest of the apparatus comprising the otolith organs is the saccular macula which resides within the saccule located just below the utricle. The saccule is in fluid continuity with the utricle and, therefore, also with the semicircular ducts (Wilson & Jones 1979).

The apparatus responsible for the transduction of angular head motion resides in a specific region of the semi-circular duct known as the ampulla. Each of the ducts is enlarged in one location to form the ampulla where it takes on an almost spherical shape just before entering the utricle. A sagittal section of the ampulla resembles the shape of the human kidney. Carrying this analogy one step further, the region in the ampulla which corresponds to the pelvis of the kidney is a structure called the crista. The crista extends into the lumen of the ampulla where it is encapsulated in a jelly-like structure known as the cupula (Lowenstein 1974). The cupula is a membranous structure which spans the entire cross-section of the ampulla.

In the past, there has been some controversy surrounding the manner in which the cupula is secured to the ampullary wall. Until recently, it was believed that the cupula moves like a swing door as if it were hinged at the crista. However, recent experiments conducted on the cupula of the frog suggest that the cupula is attached to the ampullary wall along its entire perimeter in such a way as to stop the endolymph from flowing past it (McLaren & Hillman 1976; McLaren 1977). By marking the cupula with droplets of oil using a micropipette, McLaren & Hillman were able to observe the relative displacement of the cupula with respect to the ampullary wall. Photographic results of their investigations showed that circulation of the endolymph resulted in a deflection of the cupula which appeared to behave like that of an elastic partition attached to the ampullary wall along its entire perimeter.

The crista, which is encapsulated by the cupula, contains on its surface a sensory epithelium which consists of innervated ciliated hair cells and supporting cells (Lowenstein 1974). It is here that the mechanical deflection of the cupula is transmitted through the deflection of hair cells to give rise to signals on the vestibular nerve. The biophysics of transduction by the sensory hair cells is discussed by Ohmori (1985), Corey & Hudspeth (1979), Bell & Holmes (1986), Hudspeth (1983) and others.

3. Brief historical overview

The biophysics of transduction by the vestibular end organ has been a subject of considerable interest since its discovery as the source of motion sensation in the late nineteenth century (Ewald 1892). The first mathematical description of angular motion sensation came with the introduction of the classical torsion-pendulum model by Steinhausen (1933). This model consists of a single-degree-of-freedom overdamped spring-mass-damper system subject to mass-proportional inertial forcing. The simplicity of the torsion-pendulum analogy provides insight into the behaviour of the semicircular canals and it remains a popular tool that is utilized to interpret the behaviour of the end organ. Several notable extensions have been made to enhance the original torsion-pendulum model by relating the geometry and structure of the semicircular canal system to mass, stiffness, damping and forcing parameters appearing in the model. Groen (1949, 1957) modelled the semicircular canal as a perfect toroid acted upon by a velocity-proportional moment induced by the viscosity of the endolymph, along with a displacement-proportional movement induced by the stiffness of the cupula. Groen's treatment relates the gross size and physical properties of the end organ to coefficients appearing in the classical torsion-pendulum model. A more rigorous approach presented by Oman, Marcus & Curthoys (1987) incorporates the morphology of the endolymphatic duct and represents the most biophysically compatible single-degree-of-freedom model of the semicircular canal. Consistent with the original torsion-pendulum, their analysis results in a second-order, lumped-parameter, mathematical model. Coefficients appearing in the model are related to the geometry and physical properties of the semicircular canal system.

All of the single-degree-of-freedom models (torsion-pendulum models) amount to a constant-coefficient, over-damped, spring-mass-damper system. These models admit two characteristic time constants. The slow time constant is dominant at low rates of acceleration and is defined by a balance between the viscous and stiffness terms. The fast time constant is dominant at high rates of acceleration and is defined by a balance between the mass and viscous terms. These two time constants characterize the behaviour of the model (Van Buskirk & Grant 1973; Van Buskirk, Watts & Liu 1976). In the middle frequency range, the velocity and phase of the model system (representing the velocity of the cupula relative to the head) align with the velocity and phase of the excitation (representing movement of the head). At low frequencies, the system is dominated by the stiffness, and the slow time constant causes a diminishment of the velocity gain and an increase in phase. At high frequencies, the system is dominated by the mass. Thus, the fast time constant causes a diminishment of the velocity gain and a decrease in phase. This dynamical behaviour is not restricted to the single-degree-of-freedom models. A detailed analysis of the fluid mechanics in a uniform toroidal duct subject to a stiffness-induced pressure gradient was presented by Van Buskirk & Grant (1973) and Van

Buskirk *et al.* (1976). Their results also predict a decrease in gain at both low and high frequencies accompanied by an increase in phase at low frequencies and a decrease in phase at high frequencies. Another detailed model of the fluid mechanics in a toroidal duct having a uniform circular cross-section was developed by Damiano (1989), in which the cupula was modelled as a linear elastic plate. A closed-form asymptotic solution was obtained describing the deflection of the cupula partition. The authors have since verified that this model exhibits the same gain and phase behaviour as all previous models.

The mechanical response of the system is related to the firing rate on the vestibular nerve through the mechano-electrical transduction of the vestibular hair cells (Ohmori 1985; Corey & Hudspeth 1977). Experimental measurements of the response on the vestibular nerve follow the mechanical response predicted by the two time-constant models at low frequencies but actually show the opposite behaviour at high frequencies (Fernandez & Goldberg 1971). The difference between the behaviour measured on the vestibular nerve and the mechanical response predicted by the models arises from two sources. First, adaptation and dynamic response of the hair cells is known to the frequency dependent (Ohmori 1985; Hudspeth 1983) and, second, the mechanical models contain simplifying assumptions and idealizations. A popular modelling approach has been to assume that the mechanical model is valid and to construct a transfer function to account for the difference between the signal on the vestibular nerve and the mechanical model response. This transfer function is described as being related to hair cell adaptation (Young & Oman 1969; Fernandez & Goldberg 1971; Wilson & Jones 1979). Based on isolated hair cell measurements, however, it is not clear that the dynamics of hair cell transduction is responsible for the wide difference between the mechanical model prediction and the vestibular nerve response (Ohmori 1985). This difference leads us to question if the models address the salient physical mechanism(s) responsible for the mechanical behaviour of the semicircular canal at high frequencies and motivates a more detailed analysis of the mechanics.

4. Model of the semicircular canal

The analysis presented herein utilizes the slender toroidal geometry to obtain a comprehensive model of the endolymphatic semicircular canal. Going beyond previous work, the three-dimensional analysis includes the frequency dependence of the endolymph velocity distribution and the fluid structure interaction at the cupula. The endolymphatic canal is modelled as a rigid duct containing a Newtonian fluid and the cupula partition is modelled as a generalized elastic plate. We assume that the partition is affixed to the wall of the duct along its entire perimeter in such a way as to preclude the fluid from flowing past it. The coupled system is reduced using perturbation methods to obtain a linear model that is easily solved using a Rayleigh–Ritz procedure. The geometry of the duct, and the physical properties of the endolymph and the partition, serve as inputs to the model.

4.1. *The endolymph fluid model*

We assume that the endolymph is an incompressible Newtonian fluid and is governed by the Navier–Stokes and continuity equations given by

$$\frac{\partial \boldsymbol{v}^*}{\partial t^*} + (\boldsymbol{v}^* \cdot \boldsymbol{\nabla}^*)\,\boldsymbol{v}^* = -\frac{1}{\rho}\boldsymbol{\nabla}^* P^* + \nu \boldsymbol{\nabla}^{*2} \boldsymbol{v}^*, \tag{1}$$

and
$$\nabla^* \cdot v^* = 0, \tag{2}$$

where the asterisk indicates that the variables are dimensional, otherwise they are non-dimensional. In the above equations, the variable v^* denotes the dimensional, vectorial velocity of the fluid referred to an inertial frame, the variable P^* represents the dimensional, fluid pressure, and the parameters ρ and ν denote the fluid density and kinematic viscosity, respectively.

As illustrated in figure 1, the semicircular canal is naturally described by locally orthogonal toroidal coordinates. For a circular duct having a constant radius of curvature and a non-uniform elliptical cross-section, the toroid is most simply described by defining two polar cross-sectional coordinates, (ρ, φ) and one streamwise coordinate, s^*. The coordinate transformations from Cartesian to toroidal coordinates (for a toroid of constant radius of curvature, $1/R$) are given by the following relationships:

$$x^* = (\rho^* \cos\varphi + R)\cos(s^*/R), \tag{3}$$

$$y^* = (\rho^* \cos\varphi + R)\sin(s^*/R), \tag{4}$$

$$z^* = \rho^* \sin\varphi. \tag{5}$$

In order to take advantage of the geometry, (1) and (2) must be recast expressly in terms of the coordinate system defined by (3), (4) and (5). The derivation of this transformation is given in Appendix A for all three coordinate directions ρ^*, φ and s^*. For brevity, we will show the results of this transformation for only one coordinate direction. The Navier–Stokes equation in the s^* direction, for the locally orthogonal toroidal coordinates, is given by

$$\frac{\partial v_s^*}{\partial t^*} + v_\rho^* \frac{\partial v_s^*}{\partial \rho^*} + \frac{v_\varphi^*}{\rho^*}\frac{\partial v_s^*}{\partial \varphi} + \frac{1}{R+\rho^*\cos\varphi}\left(R v_s^* \frac{\partial v_s^*}{\partial s^*} + v_s^*(v_\rho^*\cos\varphi - v_\varphi^*\sin\varphi) + \frac{R}{\rho}\frac{\partial P^*}{\partial s^*}\right)$$

$$= \nu\left(\frac{\partial^2 v_s^*}{\partial \rho^{*2}} + \frac{1}{\rho^{*2}}\frac{\partial^2 v_s^*}{\partial \varphi^2}\right) + \frac{\nu}{\rho^{*2}(R+\rho^*\cos\varphi)^2}\left\{R^2\rho^{*2}\frac{\partial^2 v_s^*}{\partial s^{*2}} + 2R\rho^{*2}\left(\cos\varphi\frac{\partial v_\rho^*}{\partial s^*} - \sin\varphi\frac{\partial v_\varphi^*}{\partial s^*}\right)\right.$$

$$\left. - \rho^{*2} v_s^* - \rho^* \sin\varphi(R+\rho^*\cos\varphi)\frac{\partial v_s^*}{\partial \varphi} + \rho^*(R^2 + 3R\rho^*\cos\varphi + 2\rho^{*2}\cos^2\varphi)\frac{\partial v_s^*}{\partial \rho^*}\right\}, \tag{6}$$

and the scalar continuity equation in toroidal coordinates is given by

$$\frac{\partial v_\rho^*}{\partial \rho^*} + \left(\frac{R+2\rho^*\cos\varphi}{R+\rho^*\cos\varphi}\right)\frac{v_\rho^*}{\rho^*} + \frac{1}{\rho^*}\frac{\partial v_\varphi^*}{\partial \varphi} + \frac{1}{R+\rho^*\cos\varphi}\left(R\frac{\partial v_s^*}{\partial s^*} - v_\varphi^*\sin\varphi\right) = 0. \tag{7}$$

The independent variables are non-dimensionalized by defining the dimensionless variables

$$\rho = \rho^*/a_0; \quad s = s^*/l; \quad t = \omega t^*, \tag{8}$$

where a_0 is the characteristic cross-sectional radius of the duct, l is the length of the loop of the duct and ω is the characteristic forcing frequency of oscillation of the duct. The length of the loop, l, is defined as

$$l = \int_0^{2\pi} \mathrm{d}s', \tag{9}$$

where s' is the curvilinear path described by the central streamline of the vestibular canal. This differs from the coordinate line s^* since s^* is a circular path chosen so as to assure local orthogonality with the other coordinates, ρ^* and φ. The characteristic radius of the loop, R, used in the transformation equations given by (3), (4) and (5) is determined from the length of the loop, l, by $R = l/2\pi$.

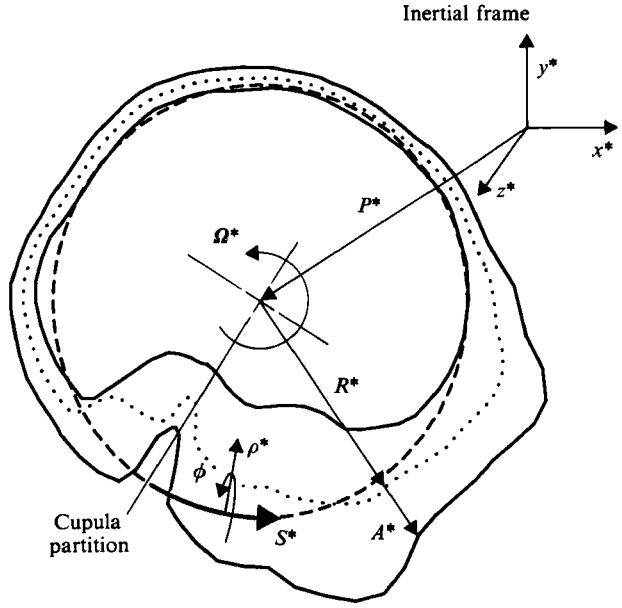

FIGURE 1. Schematic showing the geometry and notation used in the hydroelastic model of the endolymphatic semicircular canal. A photomicrograph, recorded by Curthoys & Oman (1987) perpendicularly to the human horizontal semicircular duct, was digitized and traced to determine the geometry (solid lines). The dashed circle defines the centreline of the toroidal coordinate system used in the analysis and the dotted line shows the centreline of the duct. The cupula partition is located at $s^* = 0$.

Similarly, the dependent variables may be expressed in non-dimensional form by defining

$$v_\rho = v_\rho^*/U; \quad v_\varphi = v_\varphi^*/U; \quad v_s = v_s^*/U; \quad P = P^*/\hat{P}, \tag{10}$$

where U is the characteristic velocity of the duct, and $\hat{P}$ is the characteristic pressure in the duct. The slenderness ratio, defined by the ratio of a_0 over l, can be exploited to form the asymptotic expansion parameter, ϵ. The characteristic pressure is dependent upon the characteristic velocity and slenderness ratio. It is determined by balancing the *distinguished* terms in the governing non-dimensional fluid equations (Kevorkian & Cole 1981). Expanding the resulting non-dimensional equations in ϵ and collecting terms provide the following results:

momentum equation in the ρ-direction

$$\frac{a_0^2\omega}{\nu}\frac{\partial v_\rho}{\partial t}+\frac{Ua_0}{\nu}\left(v_\rho\frac{\partial v_\rho}{\partial\rho}+\frac{v_\varphi}{\rho}\frac{\partial v_\rho}{\partial\varphi}-\frac{v_\varphi^2}{\rho}\right)-\frac{1}{\rho}\frac{\partial v_\rho}{\partial\rho}+\frac{v_\rho}{\rho^2}+\frac{2}{\rho^2}\frac{\partial v_\varphi}{\partial\varphi}-\frac{1}{\rho^2}\frac{\partial^2 v_\rho}{\partial\varphi^2}-\frac{\partial^2 v_\rho}{\partial\rho^2}+\frac{\hat{P}a_0}{\rho U\nu}\frac{\partial P}{\partial\rho}$$
$$+\left\{\frac{Ua_0}{\nu}\left(-v_s^2\cos\varphi+\frac{v_s}{2\pi}\frac{\partial v_\rho}{\partial s}\right)-\frac{v_\varphi\sin\varphi}{\rho}+\frac{\sin\varphi}{\rho}\frac{\partial v_\rho}{\partial\varphi}-\cos\varphi\frac{\partial v_\rho}{\partial\rho}\right\}2\pi\epsilon+O(\epsilon^2)=0; \tag{11}$$

momentum equation in the φ-direction

$$\frac{a_0^2\omega}{\nu}\frac{\partial v_\varphi}{\partial t}+\frac{Ua_0}{\nu}\left(v_\rho\frac{\partial v_\varphi}{\partial\rho}+\frac{v_\varphi}{\rho}\frac{\partial v_\varphi}{\partial\varphi}+\frac{v_\varphi v_\rho}{\rho}\right)-\frac{1}{\rho}\frac{\partial v_\varphi}{\partial\rho}+\frac{v_\varphi}{\rho^2}-\frac{2}{\rho^2}\frac{\partial v_\rho}{\partial\varphi}-\frac{1}{\rho^2}\frac{\partial^2 v_\varphi}{\partial\varphi^2}-\frac{\partial^2 v_\varphi}{\partial\rho^2}+\frac{\hat{P}a_0}{\rho U\nu}\frac{1}{\rho}\frac{\partial P}{\partial\varphi}$$
$$+\left\{\frac{Ua_0}{\nu}\left(v_s^2\sin\varphi+\frac{v_s}{2\pi}\frac{\partial v_\varphi}{\partial s}\right)+\frac{v_\rho\sin\varphi}{\rho}+\frac{\sin\varphi}{\rho}\frac{\partial v_\varphi}{\partial\varphi}-\cos\varphi\frac{\partial v_\varphi}{\partial\rho}\right\}2\pi\epsilon+O(\epsilon^2)=0; \tag{12}$$

momentum equation in the s-direction

$$\frac{a_0^2\omega}{\nu}\frac{\partial v_s}{\partial t}+\frac{Ua_0}{\nu}\left(v_\rho\frac{\partial v_s}{\partial \rho}+\frac{v_\varphi}{\rho}\frac{\partial v_s}{\partial \varphi}\right)-\frac{1}{\rho}\frac{\partial v_s}{\partial \rho}-\frac{1}{\rho^2}\frac{\partial^2 v_s}{\partial \varphi^2}-\frac{\partial^2 v_s}{\partial \rho^2}$$
$$+\left\{\frac{Ua_0}{\nu}\left(-v_\varphi v_s\sin\varphi+v_\rho v_s\cos\varphi+\frac{v_s}{2\pi}\frac{\partial v_s}{\partial s}\right)+\frac{\sin\varphi}{\rho}\frac{\partial v_s}{\partial \varphi}\right.$$
$$\left.-\cos\varphi\frac{\partial v_s}{\partial \rho}+\frac{\hat{P}a_0}{2\pi\rho U\nu}\frac{\partial P}{\partial s}\right\}2\pi\epsilon+O(\epsilon^2)=0; \tag{13}$$

continuity equation

$$\left(\frac{v_\rho}{\rho}+\frac{1}{\rho}\frac{\partial v_\varphi}{\partial \varphi}+\frac{\partial v_\rho}{\partial \rho}\right)+\left(v_\rho\cos\varphi-v_\varphi\sin\varphi+\frac{1}{2\pi}\frac{\partial v_s}{\partial s}\right)2\pi\epsilon+\frac{1}{a_0}O(\epsilon^2)=0. \tag{14}$$

The distinguished case is associated with the characteristic pressure

$$\hat{P}=\tfrac{1}{2}\rho U^2/\epsilon. \tag{15}$$

This results in a first-order model, as ϵ approaches zero, that balances the inertia, pressure and viscous terms. The characteristic pressure, $\hat{P}$, is related to the stagnation pressure of the entire loop of fluid on the partition.

4.2. *Endolymphatic duct boundary conditions*

Figure 1 shows the duct referred to an inertial frame defined by the rectangular coordinates (x^*, y^*, z^*). The vector $\boldsymbol{P}^*$ denotes the position of the centroid of the duct with respect to the reference frame and the vector $\boldsymbol{R}^*$ denotes the position from the centroid to the central streamline of the duct. The vector $\boldsymbol{A}^*$ locates any point on the surface of a cross-section with respect to the tip of vector $\boldsymbol{R}^*$. And finally, vector $\boldsymbol{r}^*$ denotes the position of any point on the surface of a cross-section with respect to the reference frame (x^*, y^*, z^*).

The location of a point on the surface of the duct is defined by

$$\boldsymbol{r}^*=\boldsymbol{P}^*+\boldsymbol{R}^*+\boldsymbol{A}^*. \tag{16}$$

The velocity of the rigid duct wall is therefore given by

$$\boldsymbol{v}_w^*=\dot{\boldsymbol{P}}^*+\dot{\boldsymbol{\Omega}}^*\times(\boldsymbol{R}^*+\boldsymbol{A}^*), \tag{17}$$

where $\dot{\boldsymbol{\Omega}}^*$ is a function of time which represents the vectorial, angular velocity of the duct. Non-dimesionalizing the velocity of the duct wall with the characteristic velocity, U, gives

$$\boldsymbol{v}_w=\frac{\boldsymbol{v}_w^*}{U}=\frac{\dot{\boldsymbol{P}}^*}{U}+\frac{\dot{\boldsymbol{\Omega}}^*}{U}\times(\boldsymbol{R}^*+\boldsymbol{A}^*). \tag{18}$$

For angular motion of the head, the characteristic velocity is related to the amplitude of rotation, Ω_0, by $U=R\omega\Omega_0$. Substituting this for the characteristic velocity in (18) provides

$$\boldsymbol{v}_w=\dot{\boldsymbol{P}}+\frac{\dot{\boldsymbol{\Omega}}^*}{\omega\Omega_0}\times\left(\frac{\boldsymbol{R}^*}{R}+\frac{\boldsymbol{A}^*}{R}\right), \tag{19}$$

where $\dot{\boldsymbol{P}}$ is the dimensionless centroidal velocity vector defined as the ratio $\dot{\boldsymbol{P}}^*/U$.

Furthermore, this expression for the velocity of the rigid duct wall may be expanded in terms of the slenderness ratio, ϵ, by defining the dimensionless vectors

$$\boldsymbol{A} = \frac{\boldsymbol{A}^*}{a_0}; \quad \boldsymbol{R} = \frac{\boldsymbol{R}^*}{R}; \quad \dot{\boldsymbol{\Omega}} = \frac{\dot{\boldsymbol{\Omega}}^*}{\omega \Omega_0}. \tag{20}$$

Thus, the velocity of the rigid duct wall is given in general form by the expression

$$\boldsymbol{v}_w = \dot{\boldsymbol{P}} + \dot{\boldsymbol{\Omega}} \times (\boldsymbol{R} + 2\pi\epsilon \boldsymbol{A}). \tag{21}$$

4.3. *The cupula partition*

The cupula is modelled as a flexible partition that responds to transverse pressure according to the general expression

$$\mathbf{M}^*[\boldsymbol{w}^*] = \Delta P^* \boldsymbol{n}_p, \tag{22}$$

where $\boldsymbol{n}_p$ is the outward normal to the surface of the partition, $\mathbf{M}^*$ is a matrix of differential operators and $\boldsymbol{w}^*$ is the vector displacement field of the partition. This form is consistent with shells sculptured of biological tissue and has been used to model the tympanic membrane (Stinson 1982). As a first attempt to include the fluid–structure interaction at the cupula, the above expression is reduced to the simplest possible form of an elastic plate with a bending stiffness D, plate thickness h, and plate density ρ_p. The transverse displacement, w_s^*, of the partition in the streamwise direction is a function of time and the cross-sectional coordinates ascribed to the plate. The equation of motion which describes the displacement is given by Kirchhoff's two-dimensional plate theory as

$$\nabla_c^{*2}(D \nabla_c^{*2} w_s^*) + \rho_p h \frac{\partial^2 w_s^*}{\partial t^{*2}} = \Delta P^*, \tag{23}$$

where ∇_c^{*2} is the dimensional Laplacian over the cross-section. The independent variables, ρ^* and t^*, are non-dimensionalized according to (8) and the dependent variables according to

$$w_s = \omega w_s^*/U; \quad P = P^*/\hat{P}, \tag{24}$$

where $\hat{P}$ is given by (15). Non-dimensionalizing (23) according to these definitions provides

$$\nabla_c^2(\psi \nabla_c^2 w_s) + \zeta \frac{\partial^2 w_s}{\partial t^2} = \Delta P, \tag{25}$$

where the dimensionless bending stiffness, ψ, and mass, ζ, are given by

$$\psi = \frac{UD}{a_0^4 \omega \hat{P}}; \quad \zeta = \frac{\rho_p h \omega U}{\hat{P}}. \tag{26}$$

4.4. *Boundary conditions around the periphery of the cupula*

Based on our discussion in §2 regarding the work of McLaren (1977) and McLaren & Hillman (1976), we assume that the partition is clamped to the ampullary wall along its entire perimeter. This condition requires that the partition must support the bending moment at its perimeter of attachment and thus the gradient of its displacement in the direction normal to the duct wall evaluated at the surface of the duct must be zero. In addition, the displacement of the partition along its perimeter of attachment must be zero relative to the duct wall; or equivalently, the velocity

of the partition along its perimeter of attachment must be given by the velocity of the duct wall. Mathematically, the boundary conditions around the periphery of the cupula require that

$$(\nabla_c w_s \cdot \boldsymbol{n}_w)|_\sigma = 0, \tag{27}$$

where $\boldsymbol{n}_w$ is the unit vector normal to the duct wall, and

$$\left.\frac{\partial w_s}{\partial t}\right|_\sigma = \boldsymbol{v}_w \cdot \boldsymbol{n}_p. \tag{28}$$

5. Asymptotic solution for pure rotation

The analysis up to this point is valid for any motion of the duct. The special case of pure rotation about the centroidal axis which is perpendicular to the plane of the duct is particularly relevant to the dynamics of the semicircular canals and is treated in detail here.

5.1. *Asymptotic expansion*

For this case, we assume a solution of the form of an asymptotic series expansion in terms of the slenderness ratio, ϵ, where the dependent variables of fluid velocity, partition displacement and pressure appearing in (11), (12), (13), (14) and (25) are expressed as

$$v_\rho = \epsilon v_{\rho 1} + \epsilon^2 v_{\rho 2} + \ldots, \tag{29}$$

$$v_\varphi = \epsilon v_{\varphi 1} + \epsilon^2 v_{\varphi 2} + \ldots, \tag{30}$$

$$v_s = v_{s0} + \epsilon v_{s1} + \epsilon^2 v_{s2} + \ldots, \tag{31}$$

$$w_s = w_{s0} + \epsilon w_{s1} + \epsilon^2 w_{s2} + \ldots, \tag{32}$$

$$P = P_0 + \epsilon P_1 + \epsilon^2 P_2 + \ldots. \tag{33}$$

Near the ampulla, where the cross-sectional size changes rapidly, transverse velocity components increase in magnitude causing an increase in the influence of convective nonlinearities contained in the $O(\epsilon)$ terms. This effect is not included in the $O(1)$ problem – the solution must be carried to $O(\epsilon)$ to address the convective nonlinearity.

Making these substitutions into (11), (12), (13) and (14), and using (15), provide the governing fluid equation:

$$\pi Re \frac{\partial P_0}{\partial \rho} + \left\{\pi Re \frac{\partial P_1}{\partial \rho}\right\} 2\pi\epsilon + \left\{St \frac{\partial v_{\rho 1}}{\partial t} + Re\left(v_{\rho 1}\frac{\partial v_{\rho 1}}{\partial \rho} + \frac{v_{\varphi 1}}{\rho}\frac{\partial v_{\rho 1}}{\partial \varphi} - \frac{v_{\varphi 1}^2}{\rho} + \pi \frac{\partial P_2}{\partial \rho}\right)\right.$$
$$\left. - \frac{\partial}{\partial \rho}\left(\frac{1}{\rho}\frac{\partial}{\partial \rho}(\rho v_{\rho 1})\right) - \frac{1}{\rho^2}\frac{\partial^2 v_{\rho 1}}{\partial \varphi^2} + \frac{2}{\rho^2}\frac{\partial v_{\varphi 1}}{\partial \varphi}\right\}(2\pi\epsilon)^2 + O(\epsilon^3) = 0, \tag{34}$$

$$Re\frac{\pi}{\rho}\frac{\partial P_0}{\partial \varphi} + \left\{Re\frac{\pi}{\rho}\frac{\partial P_1}{\partial \varphi}\right\} 2\pi\epsilon + \left\{St\frac{\partial v_{\varphi 1}}{\partial t} + Re\left(v_{\rho 1}\frac{\partial v_{\varphi 1}}{\partial \rho} + \frac{v_{\varphi 1}}{\rho}\frac{\partial v_{\varphi 1}}{\partial \varphi} + \frac{v_{\varphi 1}v_{\rho 1}}{\rho} + \frac{\pi}{\rho}\frac{\partial P_2}{\partial \varphi}\right)\right.$$
$$\left. - \frac{\partial}{\partial \rho}\left(\frac{1}{\rho}\frac{\partial}{\partial \rho}(\rho v_{\varphi 1})\right) - \frac{2}{\rho^2}\frac{\partial v_{\rho 1}}{\partial \varphi} - \frac{1}{\rho^2}\frac{\partial^2 v_{\varphi 1}}{\partial \varphi^2}\right\}(2\pi\epsilon)^2 + O(\epsilon^3) = 0, \tag{35}$$

$$St\frac{\partial v_{s0}}{\partial t} + \frac{1}{2}Re\frac{\partial P_0}{\partial s} - \frac{1}{\rho}\frac{\partial}{\partial \rho}\left(\rho\frac{\partial v_{s0}}{\partial \rho}\right) - \frac{1}{\rho^2}\frac{\partial^2 v_{s0}}{\partial \varphi^2} + O(\epsilon) = 0, \tag{36}$$

$$\frac{v_{\rho 1}}{\rho} + \frac{1}{\rho}\frac{\partial v_{\varphi 1}}{\partial \varphi} + \frac{\partial v_{\rho 1}}{\partial \rho} + \frac{1}{2\pi}\frac{\partial v_{s0}}{\partial s} + \left\{v_{\rho 2}\cos\varphi - v_{\varphi 2}\sin\varphi + \frac{1}{2\pi}\frac{\partial v_{s1}}{\partial s}\right\} 2\pi\epsilon + \frac{1}{a}O(\epsilon^2) = 0, \tag{37}$$

where the Stokes number, St, and the Reynolds number, Re, are defined as

$$St = \frac{a_0^2 \omega}{\nu}; \quad Re = \frac{U a_0}{\nu}. \tag{38}$$

According to (34) and (35), therefore, the $O(1)$ momentum equations in the ρ- and φ-directions, are given by

$$\frac{\partial P_0}{\partial \rho} = 0; \quad \frac{\partial P_0}{\partial \varphi} = 0. \tag{39}$$

Therefore, at any instant in time, the $O(1)$ pressure remains constant over any given cross-section. According to (36), the $O(1)$ momentum equation in the s-direction takes the form

$$St \frac{\partial v_{s0}}{\partial t} - \nabla_c^2 v_{s0} + \tfrac{1}{2} Re \frac{\partial P_0}{\partial s} = 0. \tag{40}$$

5.2. *Transformation to homogenize the boundary conditions*

For the case of pure rotation, the centroidal position vector, $\boldsymbol{P}$, remains constant with time and thus $\dot{\boldsymbol{P}}$ in (21) is zero. The velocity of the rigid duct wall to an $O(1)$ approximation for pure rotation reduces to

$$\boldsymbol{v}_{w0} = \dot{\boldsymbol{\Omega}} \times \boldsymbol{R}. \tag{41}$$

For pure rotation, $\boldsymbol{R}$ is always orthogonal to the angular velocity vector $\dot{\boldsymbol{\Omega}}$, and we may write the cross-product of these two vectors in the streamwise direction as

$$v_{w0} = r(s)\, \dot{\Omega}, \tag{42}$$

where $r(s) = |\boldsymbol{R}|$ is dependent on the streamwise coordinate s and represents the local, non-dimensional radius of the duct. Enforcing the no-slip condition, we require that the tangential velocity of the fluid at a solid interface is given by the tangential velocity of the solid. Since the wall of the duct is assumed to be rigid and impermeable, the velocity of the fluid immediately adjacent to the duct wall, for pure rotation, is given to an $O(1)$ approximation by v_{w0} delineated above. Thus, the boundary condition for the equation of motion given by (40) is

$$v_{s0}|_w = r\dot{\Omega}. \tag{43}$$

This boundary condition may be homogenized by defining a new variable u, where

$$u \equiv v_s - v_s|_w, \tag{44}$$

and represents the streamwise velocity of the fluid relative to the duct wall. For pure rotation, to an $O(1)$ approximation, the relative velocity of the fluid, u_0, far from the ampulla, is given by

$$u_0 = v_{s0} - v_{s0}|_w = v_{s0} - r\dot{\Omega}. \tag{45}$$

Substituting this variable into (40) and (43) yields, respectively, the differential equation and homogeneous boundary condition for the $O(1)$ problem, under pure rotational forcing, given by

$$St \frac{\partial u_0}{\partial t} - \nabla_c^2 u_0 + \tfrac{1}{2} Re \frac{\partial P_0}{\partial s} = -St\, r\ddot{\Omega}, \tag{46}$$

$$u_0|_w = 0. \tag{47}$$

In addition to the boundary condition on the fluid, we may homogenize the boundary condition on the partition. The velocity vector of the duct wall, $\boldsymbol{v}_w$, is given to an $O(1)$ approximation, for pure rotation, to be of magnitude $r\dot{\Omega}$, and in the streamwise direction. According to (42), therefore, the clamped boundary condition on the partition, to an $O(1)$ approximation, for pure rotation becomes

$$\left.\frac{\partial w_{s0}}{\partial t}\right|_\sigma = v_{w0} = r\dot{\Omega}. \tag{48}$$

This boundary condition may be homogenized by defining a new variable, w, such that

$$\frac{\partial w}{\partial t} \equiv \frac{\partial w_s}{\partial t} - \left.\frac{\partial w_s}{\partial t}\right|_\sigma, \tag{49}$$

where w represents the transverse displacement of the partition relative to the duct wall. For pure rotation, to an $O(1)$ approximation, the relative, transverse velocity of the partition, $\partial w_0/\partial t$, is given by

$$\frac{\partial w_0}{\partial t} = \frac{\partial w_{s0}}{\partial t} - \left.\frac{\partial w_{s0}}{\partial t}\right|_\sigma = \frac{\partial w_{s0}}{\partial t} - r\dot{\Omega}, \tag{50}$$

where

$$\left.\frac{\partial w_0}{\partial t}\right|_\sigma = 0. \tag{51}$$

Since the clamped boundary condition requires the displacement of the perimeter of the partition to match the displacement of the duct wall, we may write from the previous result

$$w_0|_\sigma = 0. \tag{52}$$

Substituting this into the $O(1)$ approximation of (25), (27) and (28) yields, respectively, the differential equation and homogeneous boundary conditions for the partition under pure rotational forcing given by

$$\nabla_c^2(\psi\nabla_c^2 w_0) + \zeta\left(\frac{\partial^2 w_0}{\partial t^2} + r\ddot{\Omega}\right) = \Delta P_0, \tag{53}$$

$$(\nabla_c w_0 \cdot \boldsymbol{n}_w)|_\sigma = 0, \tag{54}$$

$$w_0|_\sigma = 0. \tag{55}$$

5.3. *Pressure acting on the cupula – general*

Our goal is to determine the deflection of the partition, which in turn provides a model to determine the deflection of the innervated hair cells within the cupula. To this end, the pressure acting on the partition must be related to endolymphatic fluid pressure. This is achieved by integrating (46) over the cross-sectional area, $A(s)$. Rearranging terms, we have

$$\frac{\partial P_0}{\partial s} = -\frac{2}{ReA}\left\{St\iint_A\left(\frac{\partial u_0}{\partial t} + r\ddot{\Omega}\right)\mathrm{d}A - \iint_A \nabla_c^2 u_0\,\mathrm{d}A\right\}. \tag{56}$$

Applying Green's theorem to the second term on the right-hand side of (56) and integrating over the length of the duct gives

$$\Delta P_0 = -\frac{2St}{Re}\left\{\ddot{\Omega}\int_0^1 r\,\mathrm{d}s + \int_0^1 \frac{1}{A}\mathrm{d}s\iint_A \frac{\partial u_0}{\partial t}\mathrm{d}A\right\} + \int_0^1 \frac{2}{ReA}\int_{\partial A} \boldsymbol{n}_w \cdot \nabla_c u_0\,\mathrm{d}\sigma\,\mathrm{d}s. \tag{57}$$

The first term accounts for pressure induced across the partition due to the inertia of the loop of fluid and the second term accounts for viscous interaction between the endolymph and the duct wall. From an $O(1)$ integral mass balance, we have

$$\frac{\partial}{\partial s}\int\int_A u_0 \,\mathrm{d}A = 0. \tag{58}$$

This implies, therefore, that at any instant in time, the integral in the above expression evaluated at any cross-section in the duct is equivalent to the same integral evaluated at any other cross-section. We also know from continuity, that the velocity of the fluid on the surface of the partition must match the partition velocity exactly. Thus we have that

$$\int\int_A u_0 \,\mathrm{d}A = \int\int_A \frac{\partial w_0}{\partial t}\mathrm{d}A. \tag{59}$$

Using this, the pressure drop across the partition is related to the relative displacement of the cupula and the motion of the head by

$$\Delta P_0 = -\frac{2St}{Re}\left\{\ddot{\Omega}\int_0^1 r\,\mathrm{d}s + \int_0^1 \frac{1}{A}\mathrm{d}s \int\int_A \frac{\partial^2 w_0}{\partial t^2}\mathrm{d}A\right\} + \int_0^1 \frac{2}{ReA}\int_{\partial A} \boldsymbol{n}_w \cdot \boldsymbol{\nabla}_c u_0 \,\mathrm{d}\sigma\,\mathrm{d}s. \tag{60}$$

5.4. *Pressure acting on the cupula – with approximate transition layer*

If we consider a transitional layer near the partition, and an outer region comprising most of the fluid loop, we can break the second term of (60) into two parts as follows:

$$\begin{aligned}\int_0^1 \frac{2}{ReA}\int_{\partial A} \boldsymbol{n}_w \cdot \boldsymbol{\nabla}_c u_0 \,\mathrm{d}\sigma\,\mathrm{d}s \\ = \underbrace{\int_0^{\delta^*} \frac{2}{ReA}\int_{\partial A} \boldsymbol{n}_w \cdot \boldsymbol{\nabla}_c u_{0_p} \,\mathrm{d}\sigma\,\mathrm{d}s + \int_{1-\delta^*}^1 \frac{2}{ReA}\int_{\partial A} \boldsymbol{n}_w \cdot \boldsymbol{\nabla}_c u_{0_p} \,\mathrm{d}\sigma\,\mathrm{d}s}_{\text{near to the partition}} \\ \underbrace{+ \int_{\delta^*}^{1-\delta^*} \frac{2}{ReA}\int_{\partial A} \boldsymbol{n}_w \cdot \boldsymbol{\nabla}_c u_{0_f} \,\mathrm{d}\sigma\,\mathrm{d}s}_{\text{away from the partition}},\end{aligned} \tag{61}$$

where δ^* is selected to represent the length of the transitional layer, u_{0_p} is the velocity of the fluid near to the partition, and u_{0_f} is the velocity of the fluid in regions of the duct which are sufficiently far from the partition so as to be unaffected by how the partition is attached to the duct wall.

For the clamped partition $(\boldsymbol{\nabla}_c w_0 \cdot \boldsymbol{n}_w)|_\sigma = 0$. As a direct result, the shear stress on the fluid along the surface of the duct wall where the partition attaches is zero. This suggests that (61) can be approximated by

$$\int_0^1 \frac{2}{ReA}\int_{\partial A} \boldsymbol{n}_w \cdot \boldsymbol{\nabla}_c u_0 \,\mathrm{d}\sigma\,\mathrm{d}s \approx \int_\delta^{1-\delta} \frac{2}{ReA}\int_{\partial A} \boldsymbol{n}_w \cdot \boldsymbol{\nabla}_c u_{0_f} \,\mathrm{d}\sigma\,\mathrm{d}s, \tag{62}$$

where δ is the *effective* length of the transition region such that $\delta < \delta^*$. This length is in some ways analogous to the effective length of the entrance region in a pipe flow (Potter & Foss 1975). With this approximation, it is not necessary to determine the details of the velocity distribution within the transition region when finding the $O(1)$

solution. Substituting this result into (60) provides the pressure gradient across the partition as

$$\Delta P_0 = -\frac{2St}{Re}\left\{\ddot{\Omega}\int_0^1 r\,\mathrm{d}s + \int_0^1 \frac{\mathrm{d}s}{A}\iint_A \frac{\partial^2 w_0}{\partial t^2}\,\mathrm{d}A\right\} + \int_\delta^{1-\delta}\frac{2}{ReA}\int_{\partial A}\boldsymbol{n}_w\cdot\nabla_c u_{0_t}\,\mathrm{d}\sigma\,\mathrm{d}s. \quad (63)$$

5.5. *Endolymphatic viscous shear stress*

Our primary goal is to determine the deflection of the cupula partition containing the innervated hair cells. The deflection is determined from (53) subject to the pressure given by (63). The pressure contains a term accounting for the viscous shear stress acting on the walls of the endolymphatic duct that depends on the fluid velocity profile, u_{0_t}.

In regions of the duct which are sufficiently far from the partition so as to be unaffected by how the partition is attached to the duct wall, we assume that the velocity profile is axisymmetric about the duct centreline and has a cross-sectional distribution of the form

$$u_{0_t} = u_1(s,t)\,u_c(\rho/a(s)), \quad (64)$$

where $u_c(\rho/a(s))$ describes the cross-sectional shape of the velocity profile and $u_1(s,t)$ describes the lengthwise and temporal variations. The radial argument of u_c has been normalized with the local, dimensionless, cross-sectional radius, $a(s) = a^*(s)/a_0$, so that it ranges from 0 to 1 for all cross-sections.

Applying the integral mass balance of (58) to u_{0_t} gives

$$\frac{\partial}{\partial s}\left\{u_1(s,t)\iint_A u_c(\rho/a(s))\,\mathrm{d}A\right\} = 0. \quad (65)$$

Performing the substitution $\rho = \eta a(s)$, where η is the normalized radial coordinate, gives

$$\frac{\partial}{\partial s}\left\{u_1(s,t)\,2\pi a^2(s)\int_0^1 u_c(\eta)\,\eta\,\mathrm{d}\eta\right\} = 0. \quad (66)$$

Since the integral in the above expression is invariant, we have

$$\frac{\partial}{\partial s}(u_1(s,t)\,A(s)) = 0, \quad (67)$$

so $u_1(s,t)$ is inversely proportional to the cross-sectional area, $A(s)$, such that

$$u_1(s,t) = \frac{f(t)}{A(s)}. \quad (68)$$

Using (59) and (68), the time dependence of u_1 is found to be

$$f(t) = \frac{\iint_A \frac{\partial w_0}{\partial t}\,\mathrm{d}A}{2\int_0^1 u_c(\eta)\,\eta\,\mathrm{d}\eta}. \quad (69)$$

Substituting this into (64) we find

$$u_{0_t} = \frac{\iint_A \frac{\partial w_0}{\partial t}\,\mathrm{d}A}{2A(s)\int_0^1 u_c(\eta)\,\eta\,\mathrm{d}\eta}\,u_c(\eta). \quad (70)$$

We are now in a position to evaluate the viscous shear stress term in (63). From (70)

$$\int_{\partial A} \boldsymbol{n}_w \cdot \nabla_c u_{0_f} \, d\sigma = \frac{1}{a^2(s)} \frac{\iint_A \frac{\partial w_0}{\partial t} dA}{\int_0^1 u_c(\eta)\, \eta \, d\eta} u_c'(1). \tag{71}$$

Defining a dynamic shear stress velocity profile factor, λ, as the ratio of the non-dimensional slope of the velocity at the wall to the non-dimensional average velocity gives

$$\lambda \equiv \frac{-\pi \int_{\partial A} \frac{\partial u_{0_f}}{\partial \rho} d\sigma}{\iint_A u_{0_f} dA}, \tag{72}$$

and for the axisymmetric case

$$\lambda \equiv \frac{-\pi u_c'(1)}{\int_0^1 u_c(\eta)\, \eta \, d\eta}. \tag{73}$$

The factor λ accounts for the influence of the shape of the cross-sectional velocity profile on the shear stress, or viscous drag, at the wall. For a fully developed, Poiseuille flow in a straight, circular pipe, $\lambda = 8\pi$. The same value is found for fully developed, steady, laminar flow between parallel plates. As shown later in this section, for sinusoidal oscillation of the endolymphatic duct, the average value of $\lambda \sim 25.1 \sim 8\pi$ at low frequencies and increases slightly at the high physiological frequencies.

Substituting this into (63) gives the pressure acting across the cupula partition in terms of the average partition velocity and acceleration, system geometry and physical parameters. This results in

$$\Delta P_0 = -\frac{2St}{Re}\left\{\ddot{\Omega} \int_0^1 r \, ds + \int_0^1 \frac{ds}{A} \iint_A \frac{\partial^2 w_0}{\partial t^2} dA\right\} - \int_\delta^{1-\delta} \left(\frac{2\lambda}{Re\, A^2}\right) ds \iint_A \frac{\partial w_0}{\partial t} dA. \tag{74}$$

5.6. *Endolymph velocity distribution*

In the present section we obtain a closed-form description of the endolymph velocity distribution. This solution assumes that (64) applies, so the velocity distribution is not valid in the transition region near the cupula. An eigenfunction expansion is utilized to determine the cross-sectional velocity profile, $u_c(\rho/a)$, and integral continuity is applied in combination with the inertial forcing to determine the lengthwise and temporal variations of the velocity, $u_1(s,t)$.

5.6.1. *Homogeneous solution*

For the axisymmetric case, (46) is written as

$$\frac{1}{\rho}\frac{\partial}{\partial \rho}\left(\rho \frac{\partial u_0}{\partial \rho}\right) - St \frac{\partial u_0}{\partial t} = \tfrac{1}{2} Re \frac{\partial P_0}{\partial s} + St\, r \ddot{\Omega}. \tag{75}$$

We can interpret the right-hand side as a forcing function dependent on s and t. If we consider only the homogeneous part we have

$$\frac{1}{\rho}\frac{\partial}{\partial \rho}\left(\rho \frac{\partial u_0}{\partial \rho}\right) - St \frac{\partial u_0}{\partial t} = 0. \tag{76}$$

Separating variables as in (64), where the velocity distribution outside of the transition region is

$$u_{0_t} = u_1(s,t)\,u_c(\eta), \tag{77}$$

and taking $\eta = \rho/a(s)$, we have

$$\frac{\frac{1}{\eta}\frac{\partial}{\partial\eta}\left(\eta\frac{\partial u_c}{\partial\eta}\right)}{u_c} = \frac{St\,a^2\frac{\partial u_1}{\partial t}}{u_1} = -\beta^2. \tag{78}$$

We now see that the differential equation governing u_c is Bessel's equation given by

$$\frac{1}{\eta}\frac{\partial}{\partial\eta}\left(\eta\frac{\partial u_c}{\partial\eta}\right)+\beta^2 u_c = 0. \tag{79}$$

The boundary condition given by (47) may be rewritten in terms of u_c as

$$u_c|_{\eta=1} = 0. \tag{80}$$

The solution to the homogeneous equation takes the form

$$u_{c_n}\left(\frac{\rho}{a}\right) = J_0\left(\frac{\beta_n\rho}{a}\right), \tag{81}$$

where β_n are the eigenvalues such that $J_0(\beta_n) = 0$. Writing u_{0_t} as an eigenfunction expansion in terms of u_{c_n} provides

$$u_{0_t} = \sum_{n=1}^{\infty} u_{1_n}(s,t)\,u_{c_n}(\rho/a) = \sum_{n=1}^{\infty} u_{1_n}(s,t)\,J_0\left(\frac{\beta_n\rho}{a}\right). \tag{82}$$

5.6.2. *Inhomogeneous solution for sinusoidal motion*

Substituting (82) into (75) we have

$$\sum_{n=1}^{\infty}\left\{\beta_n^2 J_{0_n} u_{1_n} + St\,J_{0_n}\frac{\partial u_{1_n}}{\partial t}\right\} = g(s)\,e^{it}, \tag{83}$$

where $J_{0_n} = J_0(\beta_n\rho/a)$ and we have assumed sinusoidal motion such that

$$\tfrac{1}{2}Re\frac{\partial P_0}{\partial s} + Str\,\ddot{\Omega} = -g(s)\,e^{it}. \tag{84}$$

If we multiply (83) by the orthogonal function J_{0_m}, integrate the expression over the cross-section and simplify using the orthogonality of the Bessel functions we obtain

$$\frac{\partial u_{1_n}}{\partial t} + \alpha_n u_{1_n} = g_n e^{it}, \tag{85}$$

where

$$\alpha_n = \beta_n^2/St, \tag{86}$$

and

$$g_n = g_n(s) = \frac{g(s)\langle 1, J_{0_n}\rangle}{St\langle J_{0_n}, J_{0_n}\rangle}, \tag{87}$$

where the inner product is defined by

$$\langle f, g\rangle = \iint_A fg\,dA. \tag{88}$$

The general solution of (85) is

$$u_{t_n}(s,t) = \frac{g_n}{\alpha_n + \mathrm{i}} e^{\mathrm{i}t} + u_{1_0} e^{-\alpha_n t}. \tag{89}$$

After transients from the initial conditions die out

$$u_{0_r}(\rho, s, t) = g(s)\, e^{\mathrm{i}t} \left\{ \sum_{n=1}^{\infty} \frac{J_{0_n}}{\beta_n^2 + \mathrm{i}St} \frac{\langle 1, J_{0_n} \rangle}{\langle J_{0_n}, J_{0_n} \rangle} \right\}. \tag{90}$$

The cross-sectional shape of the velocity distribution is given by the sum of the Bessel functions and the variation in amplitude along the length is given by the function $g(s)$. Substitution into (58) determines $g(s)$. The velocity distribution at two frequencies is shown in figure 3 below.

For this distribution, the shear stress velocity profile factor λ appearing in (74) and defined by (73) is

$$\lambda = \frac{-\pi \sum_{n=1}^{\infty} J_0'(\beta_n) \dfrac{\langle 1, J_{0_n} \rangle}{\langle J_{0_n}, J_{0_n} \rangle} \dfrac{\beta_n}{(\beta_n^2 + \mathrm{i}St)}}{\sum_{n=1}^{\infty} \dfrac{\langle 1, J_{0_n} \rangle}{(\beta_n^2 + \mathrm{i}St) \langle J_{0_n}, J_{0_n} \rangle}}, \tag{91}$$

and is shown as a function of frequency in figure 4 below. With this result, the combination of (53) and (74), together with the boundary conditions, provide a closed model to determine the dynamic deflection of the cupula partition.

5.7. *Model governing deflection of the partition*

The resulting model is obtained by substituting (74) for the pressure difference across the partition into the momentum equation of the partition, given by (53). Rearranging and collecting terms gives

$$\zeta \frac{\partial^2 w_0}{\partial t^2} + \frac{2St}{Re} \int_0^1 \frac{1}{A} \mathrm{d}s \iint_A \frac{\partial^2 w_0}{\partial t^2} \mathrm{d}A + \frac{2\lambda}{Re} \int_\delta^{1-\delta} \frac{1}{A^2} \mathrm{d}s \iint_A \frac{\partial w_0}{\partial t} \mathrm{d}A + \nabla_c^2 (\psi \nabla_c^2 w_0)$$
$$= -\left(\frac{2St}{Re} \int_0^1 r \, \mathrm{d}s + \zeta r \right) \ddot{\Omega}, \tag{92}$$

subject to the clamped boundary conditions given by (54) and (55). This equation accounts for: (i) inertia of the fluid in the variable cross-sectional duct, (ii) frequency-dependent viscous shear stress on the wall of the variable cross-sectional duct, (iii) frequency-dependent fluid velocity profile for sinusoidal oscillation, (iv) inertia of the partition structure, (v) variable stiffness of the partition, and (vi) the distorted toroidal geometry of the system.

Consistent with Oman *et al.* (1987), the effective inertia of the fluid at the partition is proportional to the integral of $1/A$ while the effective viscous drag is proportional to the integral of $1/A^2$. The velocity distribution obtained outside the transition region is also consistent with the work of Van Buskirk *et al.* (1976) and Van Buskirk (1977, 1987). The incorporation of an effective transition length, δ, enabled us to determine the pressure acting across the cupula without detailing the velocity distribution in the transition region near the cupula. In fact, since the coefficient to the viscous term varies like the integral of $1/A^2$, the results are extremely insensitive

to the length of the transition region due to the large cross-sectional ares on both sides of the cupula. Going beyond previous work, this model includes the spatial distribution of the cupula deflection and resulting fluid–structure interaction.

6. Rayleigh–Ritz solution

The deflection of the partition is determined by solving (92) using a Rayleigh–Ritz method. The partition deflection is written in the form

$$w_0(\rho,\varphi,t) = \sum_{n-1}^{\infty} T_n(t)\, q_n(\rho,\varphi), \tag{93}$$

where $q_n(\rho,\varphi)$ are comparison functions meeting the essential boundary conditions of the partition (Reddy 1984). Substituting this into (92), multiplying by $q_m(\rho,\varphi)$ and integrating over the cross-section gives

$$\sum_{n-1}^{\infty}\left\{\left(\zeta\langle q_m, q_n\rangle + \frac{2St}{Re}\int_0^1 \frac{1}{A}\,\mathrm{d}s\,\bar{q}_m\,\bar{q}_n\right)\frac{\mathrm{d}^2T_n}{\mathrm{d}t^2} + \left(\frac{2\lambda}{Re}\int_0^1 \frac{1}{A^2}\,\mathrm{d}s\,\bar{q}_m\,\bar{q}_n\right)\frac{\mathrm{d}T_n}{\mathrm{d}t} + \langle q_m, \nabla_c^2(\psi\nabla_c^2 q_n)\rangle\, T_n\right\} = -\left(\frac{2St}{Re}\int_0^1 r\,\mathrm{d}s + \zeta r\right)\ddot{\Omega}\,\bar{q}_m, \tag{94}$$

where

$$\bar{q}_m = \langle 1, q_m\rangle. \tag{95}$$

Truncating the sum, (94) can be rewritten in the following matrix form:

$$\boldsymbol{M}\frac{\mathrm{d}^2\tilde{\boldsymbol{T}}}{\mathrm{d}t^2} + \boldsymbol{C}\frac{\mathrm{d}\tilde{\boldsymbol{T}}}{\mathrm{d}t} + \boldsymbol{K}\tilde{\boldsymbol{T}} = \tilde{\boldsymbol{P}}, \tag{96}$$

where $\tilde{\boldsymbol{T}}$ and $\tilde{\boldsymbol{P}}$ are vectors containing the elements T_n and P_n, respectively, and $\boldsymbol{M}$, $\boldsymbol{C}$ and $\boldsymbol{K}$ are the mass, damping and stiffness matrices, respectively. The elements of the matrix coefficients and the forcing vector are

$$M_{mn} = \zeta\langle q_m, q_n\rangle + \frac{2St}{Re}\int_0^1 \frac{1}{A}\,\mathrm{d}s\,\bar{q}_m\,\bar{q}_n, \tag{97}$$

$$C_{mn} = \frac{2\lambda}{Re}\int_0^1 \frac{1}{A^2}\,\mathrm{d}s\,\bar{q}_m\,\bar{q}_n, \tag{98}$$

$$K_{mn} = \langle q_m, \nabla_c^2(\psi\nabla_c^2 q_n)\rangle, \tag{99}$$

$$P_n = -\left(\frac{2St}{Re}\int_0^1 r\,\mathrm{d}s + \zeta r\right)\ddot{\Omega}\bar{q}_n. \tag{100}$$

Using Green's theorem and the boundary conditions, the inner products can be simplified and shown to be self-adjoint. For the case of sinusoidal motion,

$$\ddot{\Omega} = \Omega_0 \mathrm{e}^{\mathrm{i}t}. \tag{101}$$

After transients, the response of the partition can be written as

$$\tilde{\boldsymbol{T}}(t) = \tilde{\boldsymbol{A}}\mathrm{e}^{\mathrm{i}t}. \tag{102}$$

Substituting this into (96) and solving for $\tilde{\boldsymbol{A}}$ gives

$$\tilde{\boldsymbol{A}} = (-\boldsymbol{M} + \mathrm{i}\boldsymbol{C} + \boldsymbol{K})^{-1}\tilde{\boldsymbol{P}}, \tag{103}$$

n	i	j	k	$\frac{\rho}{a}\beta_{ij}^0$	α_{ij}
1	1	0	1	3.18	0.556×10^{-1}
2	1	1	1	4.59	0.152×10^{-1}
3	1	1	2	4.59	0.152×10^{-1}
4	1	2	1	5.88	0.523×10^{-2}
5	1	2	2	5.88	0.523×10^{-2}
6	2	0	1	6.28	-0.252×10^{-2}
7	1	3	1	7.12	0.201×10^{-2}
8	1	3	2	7.12	0.201×10^{-2}
9	2	1	1	7.78	-0.607×10^{-3}
10	2	1	2	7.78	-0.607×10^{-3}
11	1	4	1	8.32	0.827×10^{-3}
12	1	4	2	8.32	0.827×10^{-3}
13	2	2	1	9.17	-0.175×10^{-3}
14	2	2	2	9.17	-0.175×10^{-3}
15	3	0	1	9.42	0.110×10^{-3}
16	1	5	1	9.49	0.356×10^{-3}
17	1	5	2	9.49	0.356×10^{-3}
18	2	3	1	10.5	-0.564×10^{-4}
19	2	3	2	10.5	-0.564×10^{-4}
20	1	6	1	10.7	0.159×10^{-3}

TABLE 1. Comparison function indices and eigenvalues

and
$$w_0 \approx \sum_{n=1}^{N} q_n(\rho,\varphi) A_n \mathrm{e}^{\mathrm{i}t}, \tag{104}$$

For a circular partition with a clamped boundary, we select comparison functions

$$q_n(\rho,\varphi) = [J_i(\beta_{ij}^0 \rho/a) + \alpha_{ij} I_i(\beta_{ij}^0 \rho/a)] \cos\{\mathrm{i}\varphi + [1+(-1)^k]\pi/4\}, \tag{105}$$

where J_i is an integer-order Bessel function of the first kind, I_i is a modified integer-order Bessel function and β_{ij}^0 are the eigenvalues satisfying the clamped boundary condition such that

$$\left(\frac{\mathrm{d}I_i}{\mathrm{d}\rho} J_i + \frac{\mathrm{d}J_i}{\mathrm{d}\rho} I_i\right)_{\rho=a} = 0. \tag{106}$$

The constants α_{ij} are given by

$$\alpha_{ij} = -\left(\frac{J_i}{I_i}\right)_{\rho=a}. \tag{107}$$

For the axisymmetric case, $i = 0$ and $k = 1$. The indices i, j and k are related to the index n such that the eigenvalues, β_{ij}^0, increase with increasing n (see table 1). The comparison functions are shown by Rabbitt & Friedrich (1991).

7. Discussion of parameters for the infant human semicircular canal

Physical and geometrical parameters appearing in the model are listed in tables 2 and 3. The density and the viscosity of endolymph are taken to be similar to that of water (Steer 1967; Money *et al.* 1971). The density of the cupula is assumed to be slightly larger than the density of water and is listed in table 2. The influence of the mass of the cupula is extremely small in comparison to the mass of the endolymph;

Parameter or property	Symbol	value
Characteristic cross-sectional radius	a_0	0.054 cm
Cross-sectional radius of cupula	a_p	0.110 cm
Length of duct	l	2.402 cm
Characteristic radius of loop	R	0.382 cm
Slenderness ratio	ϵ	0.0225
Fluid density	ρ	1.0 g/cm^3
Partition density	ρ_p	1.2 g/cm^3
Partition thickness	h	0.05 cm
Bending stiffness	D	1×10^{-3} dyn cm
Fluid viscosity	ν	0.01002 cm^2/s

TABLE 2. Physical parameters and properties of the vestibular canal, endolymphatic fluid and cupula partition

Coefficient	Symbol	Value
Average velocity profile factor	λ	26
Mass coefficient	$\int_0^1 \frac{1}{A} ds$	1.30×10^3 cm$^{-1} \times a_0^2/l$
Viscosity coefficient	$\int_0^1 \frac{\lambda}{A^2} ds$	3.43×10^7 cm$^{-3} \times a_0^4/l$
Forcing coefficient	$\int_0^1 r\, ds$	0.84 cm$^2 \times 2\pi/l^2$

TABLE 3. Integral coefficients to the differential terms appearing in (92)

consequently, the results of the analysis are insensitive to the density of the cupula. Geometrical parameters were determined from measurements of an infant human horizontal semicircular canal. The outline of the canal projected perpendicularly to the duct was determined from measurements of a photomicrograph recorded by Curthoys & Oman (1987). Points along the periphery of the endolymphatic duct were located on a computer-enhanced video image and recorded. The duct outline obtained using this method is shown in figure 1. Opposite the ampulla, the major axis of the membranous duct's cross-section is approximately perpendicular to the plane of the duct and the ratio of the minor to the major axis is approximately 0.73. Near the ampulla and the utricle the major axis lies approximately in the plane of the duct and the ratio of the minor axis to the major axis is approximately 0.5. Results are based on a three-dimensional geometry constructed by assembling a sequence of circular cross-sectional slices that define the same outline as measured from the photomicrograph. The circular cross-sections approximate the actual shape. Figure 2 shows orthographic projections of the three-dimensional geometry used to model the infant human endolymphatic duct. In this geometry, the centres of the circular cross-sections are approximated as falling within a single plane. Although the analysis is capable of addressing a more exact geometry, given the diversity in the shape of individual canals, it is not clear that such an exercise would produce any additional information. The geometry of the endolymphatic duct is manifested in the model through integral coefficients representing the influence of the fluid mass and viscosity on the motion of the cupula. This is divided into three distinct areas – the effective mass, the effective viscosity, and the inertia forcing. We discuss each of

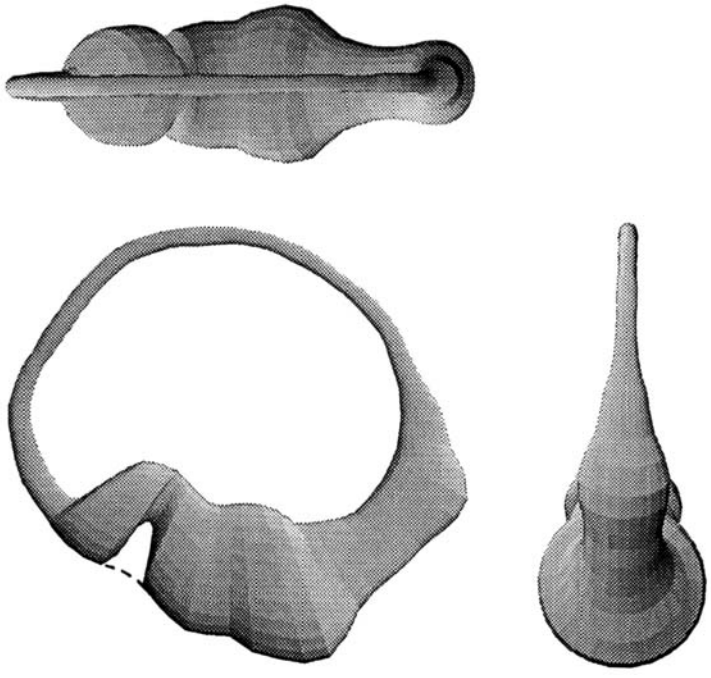

FIGURE 2. Orthographic projections of the geometry used to model the infant human horizontal canal are shown. The geometrical model consists of circular cross-sections constructed from the tracing shown in figure 1. This approximates the actual cross-sectional geometry which is roughly elliptical in shape and varies along the s^* coordinate. Although the analysis addresses the general case, results are computed for an ideal geometry where the centres of the circular cross-sections fall within a single plane.

these results separately beginning with the effective mass of the endolymph acting on the cupula.

As the duct rotates, motion of the endolymph relative to the duct wall displaces a volume that equals that displaced by the deflection of the cupula. From a frame of reference attached to the head, the endolymph moves with the deflection of the cupula. The kinetic energy of the fluid determines the influence of the entrained mass on the mass loading of the cupula. In regions where the cross-sectional area is small (in the narrow part of the duct), the fluid velocity and associated kinetic energy are large relative to regions where the duct cross-sectional area is large (in the utricle). As a result, regions of small cross-sectional area contribute more to the effective mass than regions of large cross-sectional area. The effective mass of the endolymph acting on the cupula appears as the integral of the inverse of the cross-sectional area. This integral was computed numerically and its value is given in table 3 in non-dimensional form. The inverse area dependence is consistent with the relationship obtained by Oman *et al.* (1987) using an alternative method. The result also supports the conclusion that the large cross-sectional area at the utricle does not contribute significantly to the effective mass loading of the cupula caused by the endolymph (Van Buskirk 1977). In fact, the column of endolymph in the long-and-slender region of the duct dominates the effective mass acting on the cupula.

In addition to mass loading, the endolymph induces viscous drag on the cupula. The drag is a direct result of the viscous shear stress acting between the fluid and the duct wall and is determined by the cross-sectional velocity profile. The characteristic

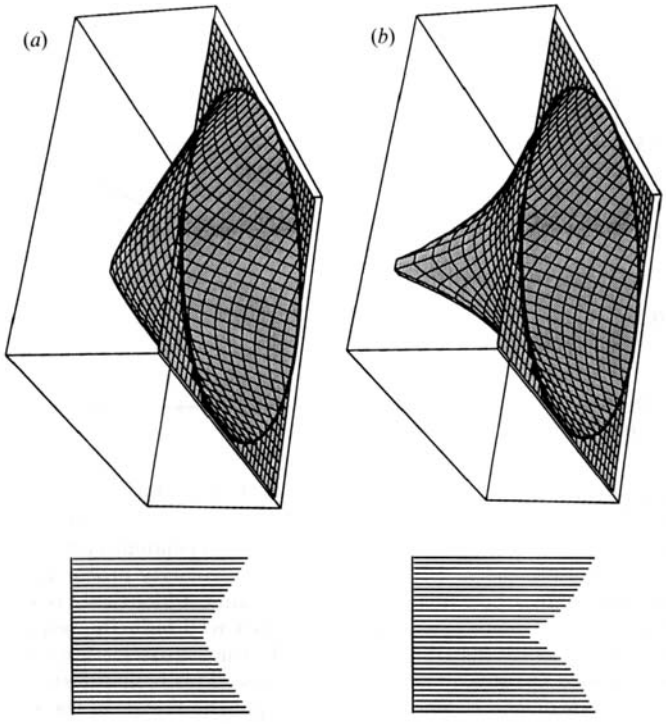

FIGURE 3. The endolymph fluid velocity profile, shown above in time averaged form at (*a*) 0.01 Hz and (*b*) 10 Hz, depends on the frequency of oscillation of the duct. At low frequencies, below 0.01 Hz, the distribution of the velocity across the cross-section is very similar to fully developed laminar flow in a straight pipe. At high frequencies, between 1 and 10 Hz, the flow becomes concentrated near the wall leaving a valley of relatively low-velocity fluid near the centre. Within the physiological range of frequencies, the shape of the velocity distribution is almost independent of time, and simply changes amplitude during the cycle. At frequencies above this range, the velocity profile changes shape significantly during the cycle. The endolymph velocity profile determines the magnitude of the viscous shear stress at the duct wall as quantified in table 3.

Reynolds number (*Re*) ranges from 0.089 at 0.01 Hz to 89 at 10 Hz, and the characteristic Stokes (*St*) number ranges from 0.025 to 25 over the same frequency range. Both *Re* and *St* are relatively low over the entire range, indicating laminar flow with only moderate frequency and phase dependence of the velocity profile. This qualitative statement is reflected quantitatively in the results. Below 1 Hz the velocity distribution is almost identical to fully developed laminar flow in a pipe of slowly varying cross-sectional area. In the endolymphatic duct, the fluid inside the duct lags the fluid contacting the duct surface. Figure 3 shows the distribution of the velocity across the circular cross-section of the model duct at two frequencies. For illustrative purposes, the magnitude of the lag in the velocity inside the duct has been exaggerated. Above 1 Hz the unsteady effect begins to play a role and influences the magnitude and phase of the shear stress at the wall. This unsteady effect is similar to that studied by Womersley (1955, 1958), and Hamakiotes & Berger (1988, 1990). When subject to harmonic motion of the head, the velocity profile in the duct exists as two distinct shapes – one in phase with the motion and one out of phase. For the range of physiological head motions (below 10 Hz) the out-of-phase component is very small in comparison to the in-phase component. The model accounts for the frequency dependence of the velocity distribution using a dynamic velocity profile

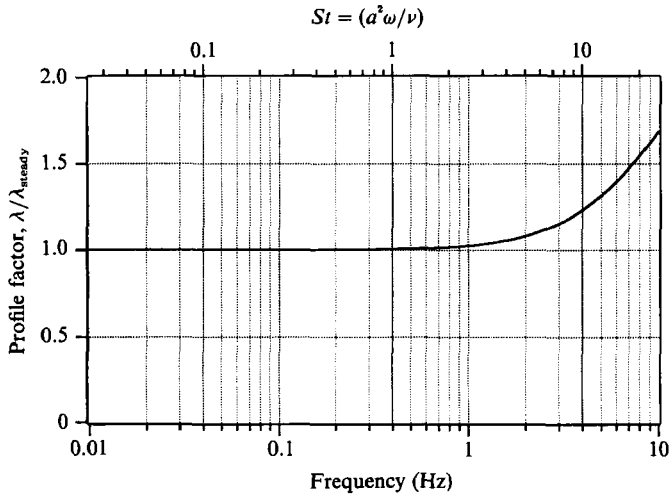

FIGURE 4. The shear stress, velocity profile factor, λ, is shown relative to the steady laminar flow value, $\lambda_{steady} = 8\pi$. This factor is a non-dimensional parameter measuring the magnitude of the shear stress relative to the volume flow rate, and is directly dependent on the shape of the velocity profile across the cross-section. Below 1 Hz, the endolymph velocity profile across the cross-section is very similar to steady laminar flow in a pipe and yields almost identical viscous effects. At higher frequencies, the fluid becomes more entrained by the duct wall inducing larger viscous effects. At 10 Hz, the change in the velocity distribution across the duct cross-section causes a 75% increase in the viscous effects above the steady laminar flow value. This is manifested as two components – one in phase and one out of phase. The in-phase component shown in the figure is the real part of λ. The out-of-phase component is the imaginary part of λ and is approximately zero over the physiological frequency range.

factor, λ, plotted in figure 4. The factor determines the magnitude and phase of the shear stress at the duct wall for a non-dimensional flow rate. Over the entire frequency range, the imaginary part of λ, corresponding to the magnitude of the out-of-phase shear stress, is negligible in comparison to the in-phase component. Below 1 Hz, the real part of λ is almost identical to that obtained from the analysis of laminar flow in a straight pipe. As shown in figure 4, the frequency dependence causes the effective viscous drag at 10 Hz to exceed the viscous drag at 1 Hz by approximately 170% for the same average flow rate. The shear stress at the wall is influenced also by the flow rate. For a given velocity profile, an increase in the flow rate causes a proportional increase in the shear stress at the wall. The shape of the velocity profile is determined by the duct geometry and the frequency while the flow rate is determined by the cross-sectional area. In the model, these factors combine to determine that the effective viscous drag on the cupula is proportional to the integral around the endolymphatic loop of the dynamic velocity profile factor divided by the square of the cross-sectional area. This integral was computed numerically and its value is given in table 3 in non-dimensional form. The cross-sectional-area dependence is consistent with Oman *et al.* (1987) and the frequency dependence is consistent with the formulation presented by Van Buskirk (1987). The asymptotic result obtained here includes both effects. In the frequency range relevant to physiological motions of the head, the morphology of the duct's cross-sectional area plays a more significant role in the behaviour of the system than the frequency dependence in the velocity profile. Similar to the effective mass loading of the cupula, the effective viscous drag is not influenced by the large cross-sectional area near the utricle. Insensitivity of the viscous drag to the flow in the utricle is a

direct result of the inverse-area dependence of the wall shear stress (see table 3). Because of this, the long and slender region of the semicircular canal is responsible for the viscous loading of the cupula.

The morphology of the cross-sectional area in the long-and-slender region of the endolymphatic duct dominates the mass and the viscous loading of the cupula. Combined with the stiffness of the cupula, the effective mass and the effective viscous drag react to inertia-induced forcing. The forcing is a result of the acceleration of the endolymphatic duct and can be calculated directly for any specific motion of the head. The results presented here are for pure harmonic rotation. For this case, the inertial forcing depends primarily on the radius from the centre of rotation out to the projection of the duct in the plane of the rotation. This result is consistent with Oman *et al.* (1987). It is noteworthy that the effective mass caused by the endolymph is proportional to the integral of the inverse area but the inertial forcing does not contain this cross-sectional-area dependence. An analogy directed at understanding the cross-sectional-area independence of the inertial forcing is provided by considering a simple hydrostatic pressure generated by the acceleration of gravity acting on a fluid in a container. The pressure in the fluid depends only on the depth and not on the shape of the container in the same way that the inertial pressure in the endolymph depends primarily on the position along the loop and not on the shape of the cross-section. This analogy applies to the pressure induced by the acceleration of the loop of endolymph if all of the fluid moves with the endolymphatic duct. Since the cupula deflects, allowing some endolymph flow relative to the duct wall, the inertial pressure is somewhat greater than the pressure acting across the cupula. The pressure drop due to the motion of the endolymph relative to the duct wall is accounted for by the aforementioned effect mass and viscous terms.

The model shows that the pressure acting across the cupula results from angular acceleration of the head. Deflection of the cupula is coupled with the flow of the endolymph relative to the duct wall. The entrained fluid causes mass and viscous loading of the cupula. The pressure induced by angular acceleration of the head is resisted by the cupula. The model assumes that the cupula traverses the duct and precludes fluid from flowing past it. As a result, the stiffness of the cupula is the primary mechanism resisting the inertially induced pressure gradient. Consequently, the stiffness of the cupula is an input to the model. It is not necessary for the stiffness to be uniform across the partition – the model includes a spatially dependent stiffness. The structure suggests that the stiffness is not homogeneous or isotropic. That is, the stiffness is expected to be substantially higher near the crista due to the rigidity of the hair cell cilia, and anisotropy is expected due to the orientation of the cilia. Inhomogeneity and anisotropy are included in the model formulation, but for simplicity in this initial presentation we have elected to present results only for the simplest case – homogeneous, isotropic bending stiffness. Direct experimental measurements of the stiffness of the human cupula are not available. Grant & Van Buskirk (1976) and Van Buskirk (1987) estimate that the global cupula stiffness, determined by the ratio of the volume displacement to the pressure gradient across the cupula, is approximately 34×10^3 dyn/cm^5. The results presented here are based on a bending stiffness determined from this global stiffness. Since the numerical value is based on indirect evidence, it represents the most uncertain numerical value utilized in the present study. For a homogeneous bending stiffness, Appendix B shows that the estimated global stiffness is equivalent to a bending stiffness D equal to 1×10^{-3} dyn cm. Results presented here are for a range of bending stiffness values from $D = 1 \times 10^{-3}$ to 5×10^{-3} dyn cm. Although the bending stiffness of the cupula is

the most uncertain parameter appearing in the model, in the middle frequency range, the deflection of the cupula predicted by the model is relatively insensitive to uncertainty in the bending stiffness.

8. Discussion of results for the infant human semicircular canal

Since the introduction of the torsion-pendulum model by Steinhausen (1933), the mechanical response of the semicircular canal has been characterized by two time constants τ_1 and τ_2. In the middle physiological frequency range, between $1/\tau_1$ and $1/\tau_2$, the classical model is dominated by a balance between the viscous drag and the inertial forcing and predicts an average cupula deflection proportional to the angular velocity of the head (constant velocity gain). At frequencies below $1/\tau_1$, a loss in gain is predicted due to the stiffness of the cupula and at frequencies above $1/\tau_2$, a loss in gain is predicted due to the mass of the endolymph (Wilson & Jones 1979; Fernandez & Goldberg 1971; Groen 1949, 1957; Van Buskirk & Grant 1973; Van Buskirk 1977). At low frequencies the firing rate measured on the vestibular nerve follows the mechanical behaviour of the cupula as predicted by the classical model, but at high frequencies the velocity gain and phase as measured on the nerve do not follow the response of the lumped-parameter torsion-pendulum model. Above 1 Hz the firing rate on the vestibular nerve actually exhibits an increase in gain and an increase in phase that is exactly the opposite of the torsion-pendulum mechanical response. Within the structure of the classical model, it is impossible to adjust the parameters to tune the mechanical behaviour of the torsion-pendulum model to follow the measured neural response. The difference between the behaviour measured on the vestibular nerve and the torsion-pendulum mechanical response has two possible sources – adaptation by the sensory hair cells, or a deficiency in the classical model at high frequencies. Experimental measurements addressing the frequency dependence of the cupula deflection could potentially resolve this question, but such a measurement is not simple and has not been reported to date. It has been argued that adaptation by the hair cells may be the main factor accounting for the difference (Young & Oman 1969; Fernandez & Goldberg 1971). Results of the analysis presented here, however, suggest that the mechanical response of the system is not predicted by the classical torsion-pendulum model at high frequencies, but rather, the mechanical response exhibits the same characteristic behaviour as the signal measured on the vestibular nerve.

The deflection of the cupula in response to sinusoidal angular motion of the head was predicted by solving the model equations over a frequency range from 0.01 Hz to 10 Hz. Results provide the velocity distribution of the endolymph in the duct, the pressure distribution, and the deflected shape of the cupula. From this, the average displacement of the cupula across the cross-section was computed. This average displacement is related to the deflection of the cilia and hence is a direct indicator of the input to the strain-sensitive hair cells. To illustrate the velocity-sensitive characteristic of the system, the average displacement was divided by the angular velocity to define the velocity gain. The velocity gain is shown in figure 5(*a*) for a sinusoidal angular oscillation of the head having a 1 rad (52.3°) zero-to-peak amplitude. Since the system is linear, doubling the amplitude will double the average displacement of the cupula. At low frequencies the mechanical response predicted by this model is very similar to the classical torsion-pendulum model and exhibits a decrease in gain due to the stiffness of the system. In the middle frequency range the gain is proportional to the velocity and the mechanical response acts as a velocity

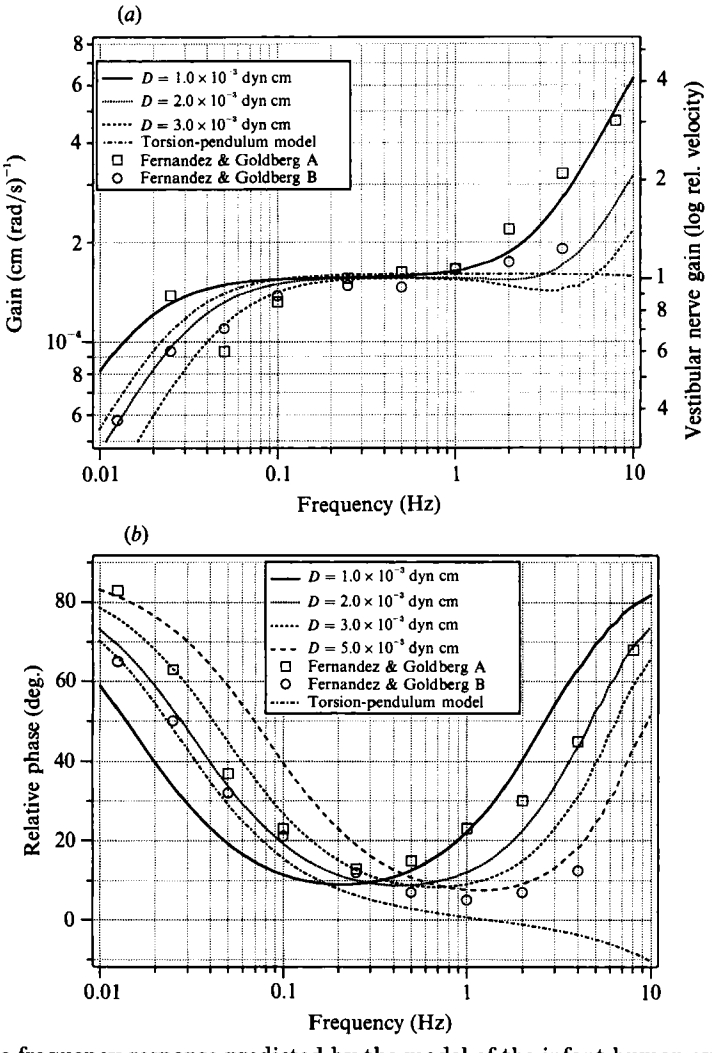

FIGURE 5. The frequency response predicted by the model of the infant human system is shown in the form of Bode plots of (*a*) the gain and (*b*) phase of the average cupula displacement relative to the zero-to-peak angular input velocity (rad/s). The gain is plotted as the log of the average displacement over the angular velocity for several partition stiffness values. The solid curve is for a bending stiffness based on the volumetric stiffness used by Van Buskirk (1987). From 0.09 to 1.5 Hz, the system acts as an angular velocity transducer with a nearly constant gain and phase. At frequencies below 0.09 Hz, the system is dominated by the partition stiffness causing a significant drop in gain and an increase in phase. Fluid inertia and viscosity combine with stiffness to cause an increase in gain and phase at frequencies above 1.5 Hz. The model result compares favourably to experimental measurements of gain and phase recorded by Fernandez & Goldberg (1971) on the vestibular nerve of the squirrel monkey (right axis). For comparison, the response of the classical torsion pendulum model is also shown. In contrast to previous mechanical models, the predicted mechanical response follows the high-frequency behaviour measured on the vestibular nerve.

transducer. Acceleration is required for sensation, but the mechanical response in the middle frequency range integrates the acceleration to produce a velocity proportional deflection of the cupula.

In contrast to the mechanical response predicted by earlier models, including the classical torsion-pendulum model, our results exhibit an increase in gain at high

physiological frequencies. The velocity gain predicted by the model is not the result of curve fitting – all of the parameters are based extensively on the three-dimensional geometry as well as on the physical properties of the endolymph and the cupula. No free parameters appear in the model. The difference between the present work and earlier results suggests that the torsion-pendulum models may lack the salient mechanism responsible for the behaviour in the high-physiological-frequency range. In fact, the slow time constant τ_2 associated with the classical model appears to have little relevance to the response in the physiological frequency range. The model presented here also shows that the gain is cut off by the mass of the system at high frequencies, but this effect occurs well above the 0.01 to 10 Hz range.

The physical mechanism responsible for the increase in gain involves the flexibility of the cupula, its interaction with the endolymph and the variable cross-sectional geometry. If the cupula were to displace like a piston, then this increase in gain would not exist. The more general approach taken by this model allows the cupula flexibility over the cross-section, thus introducing additional degrees of freedom to the mechanical response that are not accounted for in the lumped-parameter, torsion-pendulum models. These additional degrees of freedom can be viewed as introducing additional time constants. This alone, however, is not sufficient to explain the increase in gain seen in the high-frequency range since the model of Damiano (1989) exhibited a high-frequency cutoff in the gain. Indeed, this model includes a flexible partition to simulate the cupula but, owing to the idealized geometry, i.e. a toroid having a uniform circular cross-section, it overestimates the viscous forces and, to a lesser extent, the inertial forces. Like the torsion-pendulum models, however, no adjustment of the parameters can result in an increase in gain. That is to say, even after correcting the mass and viscous terms in the light of the results obtained when considering a more exact geometry, an increase in gain cannot be achieved. This suggests yet another factor to be considered which distinguishes these results from all previous models. This factor has to do with the way in which the cupula interacts with the endolymph. Specifically, the deflected shape of the cupula influences the viscous drag. In (92), the mass and viscous terms are integrated over the cross-section, while the other terms are not. This means that for certain deflected shapes of the partition, the average velocity and acceleration of the cupula could be small while the pointwise displacement is large. Under these circumstances, the stiffness term would dominate over the mass and viscous terms which in turn would lead to an increase in the gain. This characteristic, unique to this analysis, together with the variable cross-sectional geometry and a flexible cupula, account for the increase in gain in the high physiological frequencies.

The gain is shown in figure 5(*a*) for the infant human model system along with experimental data recorded by Fernandez & Goldberg (1971) on the vestibular nerve of the squirrel monkey. A direct comparison cannot be made owing to differences in the species, but the trends indicate that the mechanical gain follows the response measured on the vestibular nerve over the entire physiological frequency range more closely than predicted by the classical model. The flat gain from 0.1 to 1 Hz reflects the velocity transduction characteristic of the system. This is also illustrated in figure 6 where the average displacement of the cupula is shown as a function of frequency. To indicate the sensitivity of the behaviour to the most uncertain physical parameter appearing in the model, results are shown for several values of cupula bending stiffness.

In addition to the velocity gain, the model results in a significantly different phase than predicted by the classical torsion-pendulum at high physiological frequencies.

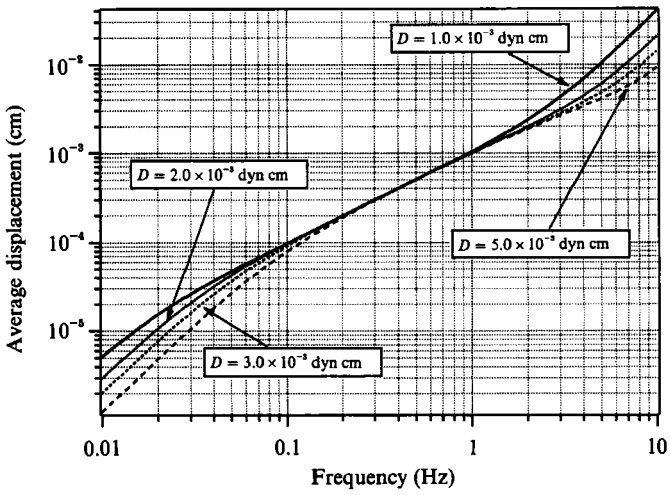

FIGURE 6. The displacement of the cupula averaged across the duct is shown as a function of frequency for the model infant human canal system. Results are shown for a sinusoidal head rotation with a peak-to-peak amplitude of 2 rad. The linearity of the curve reflects the velocity transduction characteristic of the mechanics of the canal system. The mathematical model describing the mechanics is linear, so changes in the amplitude of head rotation are reflected proportionally in the mechanical response of the cupula.

The phase of the average cupula displacement relative to the velocity of the head is shown in figure 5(*b*) for the infant human model system. Also shown as the phase recorded by Fernandez & Goldberg (1971) from the vestibular nerve of the squirrel monkey. Again, a direct comparison cannot be made owing to differences in the species, but it is interesting to note that both the model result and the experimental measurement show a phase lead starting from a maximum of 90° at low frequencies, reaching a minimum in the middle frequency range, and increasing again at high frequencies. Conforming with the velocity transduction behaviour of the system the phase is relatively flat in the middle frequency range and leads the velocity of the head by only 10°. At high physiological frequencies, an increase in the phase is predicted by the model, paralleling the behaviour measured on the vestibular nerve. This increase in the phase with increasing frequency is inconsistent with the classical torsion-pendulum model where the phase actually decreases monotonically from a lead of 90° at very low frequencies to a lag of 90° at high frequencies. The present model also shows a 90° lag at very high frequencies, but it appears well above the range of natural head motions.

9. Conclusions

A new mathematical model describing the mechanics of the vestibular semicircular canal system has been presented that includes the three-dimensional structure of the duct and the interaction of the endolymph with the cupula. The model is based extensively on the geometry of the system and on the physical properties of the endolymph and the cupula. An asymptotic analysis is applied to exploit the slender toroidal geometry of the duct. This results in a relatively simple model describing the distribution of the endolymph fluid velocity, the fluid pressure, and the deflection of the cupula. Results indicate that the mechanical response of the cupula, including

both the gain and the phase, follows the response measured on the vestibular nerve more closely than predicted by previous mechanical models. The difference is particularly pronounced at high physiological frequencies. This implies that adaptation by the vestibular hair cells may not be the primary factor responsible for the difference between prediction of the torsion-pendulum model and the high-frequency gain and phase measured on the vestibular nerve – the present analysis indicates that the frequency response measured on the nerve is primarily a reflection of the mechanical behaviour of the system. For the infant human geometry considered, the mechanical gain, defined by the average cupula displacement divided by the velocity of the head, is relatively constant in the middle frequency range from 0.1 to 1.0 Hz. In this same range the phase of the cupula displacement leads the velocity of the head by approximately 10°. Consistent with measurements on the vestibular nerve, a phase lead is predicted in the low-frequency range (0–0.1 Hz) and also in the high-frequency range (1–10 Hz). This is combined with a decrease in gain at low frequencies and an increase in gain at high frequencies.

Partial support for this work was contributed by the National Science Foundation, BCS-8957206.

Appendix A. Coordinate transformation

The Navier–Stokes and continuity equations, given in the form of (1) and (2), may be recast expressly in terms of any specific coordinate system once the various differential operators appearing on the equations are known in terms of the desired coordinates. This is accomplished for the generalized, locally orthogonal, curvilinear coordinates ξ_1, ξ_2 and ξ_3 by first obtaining the scale factors for the system. Given the transformation from rectangular coordinates (x, y, z) to the curvilinear coordinates (ξ_1, ξ_2, ξ_3) expressed in the form

$$x = x(\xi_1, \xi_2, \xi_3), \tag{A 1}$$

$$y = y(\xi_1, \xi_2, \xi_3), \tag{A 2}$$

$$z = z(\xi_1, \xi_2, \xi_3), \tag{A 3}$$

the scale factors, h_n, taken from Morse & Feshbach (1953), can be obtained for the nth coordinate direction using

$$h_n = \left[\left(\frac{\partial x}{\partial \xi_n}\right)^2 + \left(\frac{\partial y}{\partial \xi_n}\right)^2 + \left(\frac{\partial z}{\partial \xi_n}\right)^2\right]^{\frac{1}{2}}. \tag{A 4}$$

If the curvilinear coordinate unit vectors are given by $\boldsymbol{a}_1, \boldsymbol{a}_2$ and $\boldsymbol{a}_3$, the various differential operators appearing in the Navier–Stokes and continuity equations may be written in terms of this coordinate system by employing the following relationships taken from Moon & Spencer (1961) and Morse and Feshbach (1953):
the Laplacian of the vector $\boldsymbol{v}$

$$\nabla^2 \boldsymbol{v} = \nabla(\nabla \cdot \boldsymbol{v}) - \nabla \times (\nabla \times \boldsymbol{v}) = \left\{\frac{1}{h_1}\frac{\partial Y}{\partial \xi_1} + \frac{1}{h_2 h_3}\left[\frac{\partial (\Gamma)_2}{\partial \xi_3} - \frac{\partial (\Gamma)_3}{\partial \xi_2}\right]\right\} \boldsymbol{a}_1$$

$$+ \left\{\frac{1}{h_2}\frac{\partial Y}{\partial \xi_2} + \frac{1}{h_1 h_3}\left[\frac{\partial (\Gamma)_3}{\partial \xi_1} - \frac{\partial (\Gamma)_1}{\partial \xi_3}\right]\right\} \boldsymbol{a}_2 + \left\{\frac{1}{h_3}\frac{\partial Y}{\partial \xi_3} + \frac{1}{h_1 h_2}\left[\frac{\partial (\Gamma)_1}{\partial \xi_2} - \frac{\partial (\Gamma)_2}{\partial \xi_1}\right]\right\} \boldsymbol{a}_3, \tag{A 5}$$

where
$$(\Gamma)_1 = \frac{h_1}{h_2 h_3}\left\{\frac{\partial}{\partial \xi_2}(h_3 v_3) - \frac{\partial}{\partial \xi_3}(h_2 v_2)\right\}, \tag{A 6}$$

$$(\Gamma)_2 = \frac{h_2}{h_1 h_3}\left\{\frac{\partial}{\partial \xi_3}(h_1 v_1) - \frac{\partial}{\partial \xi_1}(h_3 v_3)\right\}, \tag{A 7}$$

$$(\Gamma)_3 = \frac{h_3}{h_1 h_2}\left\{\frac{\partial}{\partial \xi_1}(h_2 v_2) - \frac{\partial}{\partial \xi_2}(h_1 v_1)\right\}, \tag{A 8}$$

and
$$Y = \frac{1}{h_1 h_2 h_3}\left\{\frac{\partial}{\partial \xi_1}(h_2 h_3 v_1) + \frac{\partial}{\partial \xi_2}(h_1 h_3 v_2) + \frac{\partial}{\partial \xi_3}(h_1 h_2 v_3)\right\}; \tag{A 9}$$

the gradient of the scalar P

$$\nabla P = \sum_n \boldsymbol{a}_n \frac{1}{h_n}\frac{\partial P}{\partial \xi_n}; \tag{A 10}$$

the convective non-linearity

$$\begin{aligned}(\boldsymbol{v}\cdot\nabla)\,\boldsymbol{v} = &\left\{\left(\sum_n \frac{v_n}{h_n}\frac{\partial v_1}{\partial \xi_n}\right) + \frac{v_2}{h_1 h_2}\left(v_1\frac{\partial h_1}{\partial \xi_2} - v_2\frac{\partial h_2}{\partial \xi_1}\right) + \frac{v_3}{h_1 h_3}\left(v_1\frac{\partial h_1}{\partial \xi_3} - v_3\frac{\partial h_3}{\partial \xi_1}\right)\right\}\boldsymbol{a}_1\\ &+\left\{\left(\sum_n \frac{v_n}{h_n}\frac{\partial v_2}{\partial \xi_n}\right) + \frac{v_1}{h_1 h_2}\left(v_2\frac{\partial h_2}{\partial \xi_1} - v_1\frac{\partial h_1}{\partial \xi_2}\right) + \frac{v_3}{h_2 h_3}\left(v_2\frac{\partial h_2}{\partial \xi_3} - v_3\frac{\partial h_3}{\partial \xi_2}\right)\right\}\boldsymbol{a}_2\\ &+\left\{\left(\sum_n \frac{v_n}{h_n}\frac{\partial v_3}{\partial \xi_n}\right) + \frac{v_1}{h_1 h_3}\left(v_3\frac{\partial h_3}{\partial \xi_1} - v_1\frac{\partial h_1}{\partial \xi_3}\right) + \frac{v_2}{h_2 h_3}\left(v_3\frac{\partial h_3}{\partial \xi_2} - v_2\frac{\partial h_2}{\partial \xi_3}\right)\right\}\boldsymbol{a}_3;\end{aligned} \tag{A 11}$$

the divergence of the vector $\boldsymbol{v}$

$$\nabla\cdot\boldsymbol{v} = \frac{1}{h_1 h_2 h_3}\sum_n \frac{\partial}{\partial \xi_n}\left(h_1 h_2 h_3 \frac{v_n}{h_n}\right). \tag{A 12}$$

For the locally orthogonal, toroidal coordinate system defined by (3), (4) and (5), the scale factors, defined by (A 4), are found to be

$$h_{\rho^*} = 1 \tag{A 13}$$

$$h_{\varphi} = \rho^* \tag{A 14}$$

$$h_{s^*} = 1 + \frac{\rho^*}{R}\cos\varphi. \tag{A 15}$$

Using symbolic manipulation, these results were used in conjunction with (A 5), (A 10), (A 11) and (A 12) to obtain the Laplacian of the dimensional velocity vector, $\boldsymbol{v}^*$, the gradient of the dimensional scalar pressure, P^*, the convective nonlinearity and the divergence of the velocity vector expressly in terms of the coordinates ρ^*, φ and s^*. For the system defined by (3), (4) and (5), the terms given by (A 5), (A 10), (A 11) and (A 12) were found, in dimensional coordinates, to be:
the Laplacian of the velocity vector $\boldsymbol{v}^*$

$$[\nabla^2 \boldsymbol{v}^*]_{\rho^*} = \frac{\partial^2 v_\rho^*}{\partial \rho^{*2}} + \frac{1}{\rho^{*2}} \frac{\partial^2 v_\rho^*}{\partial \varphi^2} - \frac{2}{\rho^{*2}} \frac{\partial v_\varphi^*}{\partial \varphi} + \frac{1}{\rho^{*2}(R+\rho^* \cos\varphi)^2} \Big\{ R^2 \rho^{*2} \frac{\partial^2 v_\rho^*}{\partial s^{*2}} - 2R\rho^{*2} \cos\varphi \frac{\partial v_s^*}{\partial s^*}$$
$$+ v_\varphi^* \rho^* \sin\varphi (R + 2\rho^* \cos\varphi) - v_\rho^* (R^2 + 2R\rho^* \cos\varphi + 2\rho^{*2} \cos^2\varphi)$$
$$- \rho^* \sin\varphi (R + \rho^* \cos\varphi) \frac{\partial v_\rho^*}{\partial \varphi} + \rho^* (R^2 + 3R\rho^* \cos\varphi + 2\rho^{*2} \cos^2\varphi) \frac{\partial v_\rho^*}{\partial \rho^*} \Big\}, \quad \text{(A 16)}$$

$$[\nabla^2 \boldsymbol{v}^*]_{\varphi} = \frac{\partial^2 v_\varphi^*}{\partial \rho^{*2}} + \frac{1}{\rho^{*2}} \frac{\partial^2 v_\varphi^*}{\partial \varphi^2} + \frac{2}{\rho^{*2}} \frac{\partial v_\rho^*}{\partial \varphi} + \frac{1}{\rho^{*2}(R+\rho^* \cos\varphi)^2} \Big\{ R^2 \rho^{*2} \frac{\partial^2 v_\varphi^*}{\partial s^{*2}} + 2R\rho^{*2} \sin\varphi \frac{\partial v_s^*}{\partial s^*}$$
$$- v_\rho^* R\rho^* \sin\varphi - v_\varphi^* (R^2 + 2R\rho^* \cos\varphi + \rho^{*2}) - \rho^* \sin\varphi (R + \rho^* \cos\varphi) \frac{\partial v_\varphi^*}{\partial \varphi}$$
$$+ \rho^* (R^2 + 3R\rho^* \cos\varphi + 2\rho^{*2} \cos^2\varphi) \frac{\partial v_\varphi^*}{\partial \rho^*} \Big\}, \quad \text{(A 17)}$$

$$[\nabla^2 \boldsymbol{v}^*]_{s^*} = \frac{\partial^2 v_s^*}{\partial \rho^{*2}} + \frac{1}{\rho^{*2}} \frac{\partial^2 v_s^*}{\partial \varphi^2} + \frac{1}{\rho^{*2}(R+\rho^* \cos\varphi^2)} \Big\{ R^2 \rho^{*2} \frac{\partial^2 v_s^*}{\partial s^{*2}} + 2R\rho^{*2} \Big(\cos\varphi \frac{\partial v_\rho^*}{\partial s^*} - \sin\varphi \frac{\partial v_\varphi^*}{\partial s^*} \Big)$$
$$- \rho^{*2} v_s^* - \rho^* \sin\varphi (R + \rho^* \cos\varphi) \frac{\partial v_s^*}{\partial \varphi} + \rho^* (R^2 + 3R\rho^* \cos\varphi + 2\rho^{*2} \cos^2\varphi) \frac{\partial v_s^*}{\partial \rho^*} \Big\}; \quad \text{(A 18)}$$

the gradient of the scalar pressure P^*

$$\nabla P^* = \frac{\partial P^*}{\partial \rho^*} \boldsymbol{a}_{\rho^*} + \frac{1}{\rho^*} \frac{\partial P^*}{\partial \varphi} \boldsymbol{a}_\varphi + \frac{R}{R+\rho^* \cos\varphi} \frac{\partial P^*}{\partial s^*} \boldsymbol{a}_{s^*}; \quad \text{(A 19)}$$

the convective nonlinearity

$$[(\boldsymbol{v}^* \cdot \nabla) \boldsymbol{v}^*]_{\rho^*} = v_\rho^* \frac{\partial v_\rho^*}{\partial \rho^*} - \frac{v_\varphi^{*2}}{\rho^*} + \frac{v_\varphi^*}{\rho^*} \frac{\partial v_\rho^*}{\partial \varphi} - \frac{1}{R+\rho^* \cos\varphi} \Big(R v_s^* \frac{\partial v_\rho^*}{\partial s^*} - v_s^{*2} \cos\varphi \Big), \quad \text{(A 20)}$$

$$[(\boldsymbol{v}^* \cdot \nabla) \boldsymbol{v}^*]_{\varphi} = v_\rho^* \frac{\partial v_\varphi^*}{\partial \rho^*} + \frac{v_\rho^* v_\varphi^*}{\rho^*} + \frac{v_\varphi^*}{\rho^*} \frac{\partial v_\varphi^*}{\partial \varphi} + \frac{1}{R+\rho^* \cos\varphi} \Big(R v_s^* \frac{\partial v_\varphi^*}{\partial s^*} + v_s^{*2} \sin\varphi \Big), \quad \text{(A 21)}$$

$$[(\boldsymbol{v}^* \cdot \nabla) \boldsymbol{v}^*]_{s^*} = v_\rho^* \frac{\partial v_s^*}{\partial \rho^*} + \frac{v_\varphi^*}{\rho^*} \frac{\partial v_s^*}{\partial \varphi} + \frac{1}{R+\rho^* \cos\varphi} \Big(R v_s^* \frac{\partial v_s^*}{\partial s^*} + v_s^* (v_\rho^* \cos\varphi - v_\varphi^* \sin\varphi) \Big); \quad \text{(A 22)}$$

the divergence of the velocity vector $\boldsymbol{v}^*$

$$\nabla \cdot \boldsymbol{v}^* = \frac{\partial v_\rho^*}{\partial \rho^*} + \Big(\frac{R + 2\rho^* \cos\varphi)}{R+\rho^* \cos\varphi} \Big) \frac{v_\rho^*}{\rho^*} + \frac{1}{\rho^*} \frac{\partial v_\varphi^*}{\partial \varphi} + \frac{1}{R+\rho^* \cos\varphi} \Big(R \frac{\partial v_s^*}{\partial s^*} - v_\varphi^* \sin\varphi \Big). \quad \text{(A 23)}$$

Appendix B. Quantifying the bending stiffness of the cupula partition

It is especially difficult to measure the bending stiffness of the cupula for many reasons, not least of which is the intrinsic difference in the value it assumes between *in-vivo* and *in-vitro* measurements. It is therefore an added complication to attempt *in-vivo* measurements of this property. For these and other reasons, a direct

measurement of the bending stiffness of the cupula is not available in the literature. For the purposes of this analysis, we attempt to obtain an estimate of the bending stiffness based on volumetric stiffness estimates of the actual cupula. Van Buskirk (1987), Oman *et al.* (1985) and Van Buskirk & Grant (1973) utilize a volumetric stiffness, K, for the cupula defined as

$$K = \frac{\Delta P^*}{\Delta V^*}, \tag{B 1}$$

where ΔP^* is the pressure difference across the cupula and ΔV^* is the resulting volumetric displacement. The bending stiffness of the cupula, D, utilized in the present model is related to the volumetric stiffness, K, and can be determined from the static deflection of the cupula resulting from an applied pressure. This is to be done by solving the dimensionless $O(1)$ equation of motion of the partition given by (53). In non-dimensional form, the static version of this equation is given by

$$\nabla_c^2(\psi \nabla_c^2 w_0) = \Delta P_0. \tag{B 2}$$

For the purpose of estimating the bending stiffness, we assume that the deformation is axisymmetric and solve, through four integrations of (B 2), for the deflection of the cupula. This results in

$$w_0(\rho) = \frac{\Delta P_0}{\psi}\left[\frac{\rho^4}{64} + (k_1\rho^2 + k_3)\ln\rho + k_2\rho^2 + k_4\right], \tag{B 3}$$

where the k_n are four arbitrary constants of integration. Maintaining continuity as ρ approaches zero, and applying the clamped boundary conditions determines the constants of integration and results in

$$w_0(\rho) = \frac{\Delta P_0}{64\psi}\left(\frac{a_p}{a_0}\right)^4 (\eta^2 - 1)^2, \tag{B 4}$$

where $\eta = \rho/a_p/a_0$ is the normalized radial coordinate at the partition.

Integrating over the cross-section of the duct determines the non-dimensional volumetric displacement, ΔV_0. Solving for the dimensionless stiffness ψ gives

$$\psi = \frac{\pi}{192}\frac{\Delta P_0}{\Delta V_0}\left(\frac{a_p}{a_0}\right)^4. \tag{B 5}$$

We must relate the non-dimensional stiffness, $\Delta P_0/\Delta V_0$, to the dimensional volumetric stiffness, K. From our non-dimensionalization in §4 we write $\Delta P^* = \hat{P}\Delta P_0$ and $\Delta V^* = (a_p^2 U/w)\,\Delta V_0$.

Returning now to dimensional quantities, and using our definition of the dimensionless bending stiffness, ψ, introduced in §4, give

$$\psi = \frac{UD}{a_0^4 \omega \hat{P}} = \frac{\pi}{192} K \frac{a_p^2 U}{\hat{P}\omega}\left(\frac{a_p}{a_0}\right)^4. \tag{B 6}$$

Solving for D, we find that the bending stiffness is related to the volumetric stiffness, K, and the cupula radius by

$$D = \frac{\pi}{192} K a_p^6. \tag{B 7}$$

Based on a volumetric stiffness, K, of 3.4×10^4 (g/cm^4) s^2 (Van Buskirk 1987) and an average cupula radius of 0.11 cm results in an average bending stiffness D equal to approximately 1×10^{-3} dyn cm. We stress that this is an average across the area of the cupula.

REFERENCES

BELL, J. & HOLMES, M. H. 1986 A nonlinear model for transduction in hair cells. *Hearing Res.* **21**, 97–108.

COREY, D. P. & HUDSPETH, A. J. 1977 Sensitivity, polarity, and conductance change in the response of vertebrate hair cells to controlled mechanical stimuli. *Proc. Natl Acad. Sci. USA* **74**, 2407–2411.

COREY, D. P. & HUDSPETH, A. J. 1979 Ionic basis of the receptor potential in a vertebrate hair cell. *Nature* **281**, 675–677.

CURTHOYS, I. S. & OMAN, C. M. 1987 Dimensions of the horizontal semicircular duct, ampulla and utricle in the human. *Acta. Otolaryngol (Stockholm)* **103**, 254–261.

DAMIANO, E. R. 1989 A hydroelastic model of the dynamics in a circular duct and its description of the macromechanics in the vestibular canal. Master's thesis, Washington University.

EWALD, J. R. 1892 *Physiologische Untersuchingen uber das Endorgan des Nervus Octavus.* Wiesbaden: Bergmann.

FERNANDEZ, C. & GOLDBERG, J. M. 1971 Physiology of peripheral neurons innervating semicircular canals of the squirrel monkey. II Response to sinusoidal stimulation and dynamics of peripheral vestibular system. *J. Neurophysiol.* **34**, 661–675.

GRANT, J. W. & VAN BUSKIRK, W. C. 1976 Experimental measurement of the stiffness of the cupula. *Biophys. J.* **16**, 669–677.

GROEN, J. J. 1949 *Medische Physica; de Evenwichtszintuigen*, pp. 510–561. Amsterdam: NH Uitgeversmij.

GROEN, J. J. 1957 The mechanics of the semicircular canals. *J. Physiol. Lond.* **110**, 1–17.

HAMAKIOTES, C. C. & BERGER, S. A. 1988 Fully developed pulsatile flow in a curved pipe. *J. Fluid Mech.* **195**, 23–55.

HAMAKIOTES, C. C. & BERGER, S. A. 1990 Periodic flows through curved tubes: the effect of the frequency parameter. *J. Fluid Mech.* **210**, 353–370.

HUDSPETH, A. J. 1983 Mechanoelectrical transduction by hair cells in the acouticolateralis sensory system. *Ann. Rev. Neurosci.* **6**, 187–215.

KEVORKIAN, J. & COLE, J. D. 1981 *Perturbation Methods in Applied Mathematics.* Springer.

LOWENSTEIN, O. E. 1974 Comparative morphology and physiology. In *Handbook of Sensory Physiology.* VI/1: *Vestibular System* (ed. H. H. Kornhuber), pp. 75–115. Springer.

MCLAREN, J. W. 1977 The configuration of movement of the semicircular canal cupula. Ph.D. thesis, University of Iowa.

MCLAREN, J. W. & HILLMAN, D. E. 1976 Configuration of the cupula during endolymph pressure changes. *Neurosci. Abstr.* **3**, 544, Abstr. 1730.

MONKEY, K. E., BONEN, L., BEATTY, J. D., KUEHN, L. A., SOKOLOFF, M. & WEAVER, R. S. 1971 Physical properties of fluids and structures of vestibular apparatus of the pigeon. *Am. J. Physiol.* **110**, 140–147.

MOON, P. & SPENCER, D. E. 1961 *Field Theory for Engineers.* D. Van Nostrand.

MORSE, P. M. & FESHBACH, H. 1953 *Methods of Theoretical Physics*, Part I. McGraw-Hill.

OHMORI, H. 1985 Mechano-electrical transduction currents in isolated vestibular hair cells of the chick. *J. Physiol. Lond.* **359**, 189–217.

OMAN, C. M., MARCUS, E. N. & CURTHOYS, I. S. 1987 The influence of semicircular canal morphology on endolymph flow dynamics. *Acta Otolaryngol (Stockholm)* **103**, 1–13.

POTTER, M. C. & FOSS, J. F. 1975 *Fluid Mechanics.* Wiley.

RABBITT, R. D. & FRIEDRICH, M. T. 1991 Ear canal cross-sectional pressure distributions: Mathematical analysis and computation. *J. Acoust. Soc. Am.* **89**, 2379–2390.

REDDY, J. N. 1984 *Energy and Variational Methods in Applied Mechanics.* Wiley Interscience.

STEER, R. 1967 The influence of angular and linear acceleration and thermal stimulation on the human semicircular canal. Sc.D. thesis, MIT.

STEINHAUSEN, W. 1933 Uber die beobachtungen der cupula in den bognegangsampullen des labyrinthes des libenden hecths. *Pflugers Arch.* **232**, 500–512.

STINSON, M. R. 1982 A general acoustic network representation of the middle ear. *Can. Acoust. Assoc. Symp. on Acoustics, Toronto, Canada.*

VAN BUSKIRK, W. C. 1977 The effect of the utricle on fluid flow in the semicircular canals. *Ann. Biomed. Engng* **5**, 1–11.

VAN BUSKIRK, W. C. 1987 Vestibular mechanics. In *Handbook of Bioengineering* (ed. R. Skalak & S. Chien), pp. 31.1–31.17. McGraw Hill.

VAN BUSKIRK, W. C. & GRANT, J. W. 1973 Biomechanics of the semicircular canals. *Biomechanics Symp.* pp. 53–54. ASME.

VAN BUSKIRK, W. C., WATTS, R. G. & LIU, Y. K. 1976 The fluid mechanics of the semicircular canals. *J. Fluid Mech.* **78**, 87–98.

WILSON, V. J. & JONES, G. M. 1979 *Mammalian Vestibular Physiology*. Plenum.

WOMERSLEY, J. R. 1955 Method for the calculation of velocity, rate of flow, and viscous drag in arteries when the pressure gradient is known. *J. Physiol. Lond.* **127**, 553–563.

WOMERSLEY, J. R. 1958 Oscillatory flow in arteries I. The constrained elastic tube as a model of arterial flow and pulse transmission. *Phys. Med. Biol.* **2**, 177–187.

YOUNG, L. R. & OMAN, C. R. 1969 Model of vestibular adaptation to horizontal rotation. *Aerospace Med.* **40**, 1076–1080.